

Host Galaxies of Ultra-Strong Mg II Absorbers at $z \sim 0.7$

Labanya K. Guha,^{1*} Raghunathan Srianand,^{1†} & Patrick Petitjean^{2‡}

¹*IUCAA, Postbag 4, Ganeshkhind, Pune 411007, India*

²*Institut d’Astrophysique de Paris, Sorbonne Université and CNRS, 98bis boulevard Arago, 75014 Paris, France*

Accepted XXX. Received YYY; in original form ZZZ

ABSTRACT

We report spectroscopic identification of the host galaxies of 18 ultra-strong Mg II systems (USMgII) at $0.6 \leq z \leq 0.8$. We created the largest sample by merging these with 20 host galaxies from our previous survey within $0.4 \leq z \leq 0.6$. Using this sample, we confirm that the measured impact parameters ($6.3 \leq D[\text{kpc}] \leq 120$ with a median of 19 kpc) are much larger than expected, and the USMgII host galaxies do not follow the canonical $W_{2796} - D$ anti-correlation. We show that the presence and significance of this anti-correlation may depend on the sample selection. The $W_{2796} - D$ anti-correlation seen for the general Mg II absorbers show a mild evolution at low W_{2796} end over the redshift range $0.4 \leq z \leq 1.5$ with an increase of the impact parameters. Compared to the host galaxies of normal Mg II absorbers, USMgII host galaxies are brighter and more massive for a given impact parameter. While the USMgII systems preferentially pick star-forming galaxies, they exhibit slightly lower ongoing star-forming rates compared to main sequence galaxies with the same stellar mass, suggesting a transition from star-forming to quiescent states. For a limiting magnitude of $m_r < 23.6$, at least 29% of the USMgII host galaxies are isolated, and the width of the Mg II absorption in these cases may originate from gas flows (infall/outflow) in isolated halos of massive star-forming but not starbursting galaxies. We associate more than one galaxy with the absorber in $\geq 21\%$ cases where interactions may cause wide velocity spread.

Key words: galaxies: evolution – galaxies: groups: general – galaxies: haloes – galaxies: high-redshift – quasars: absorption lines.

1 INTRODUCTION

The formation and evolution of galaxies is one of the most fundamental problems in extragalactic astronomy. Galaxies evolution is thought to be governed by the joint action of accretion of pristine metal-poor gas from the intergalactic medium (IGM), in-situ star formation in the galactic disk, and feedback from star-formation-driven metal-rich galactic winds – a complex process known as the ‘cosmic baryon cycle’ (Anglés-Alcázar et al. 2017; Péroux & Howk 2020). The interplay between galactic winds and gas accretion from the IGM creates a metal-enriched gaseous halo surrounding galaxies out to a few virial radii known as the circumgalactic medium (CGM). The kinematically complex, multi-phase CGM, which serves as an interface between the galactic disk (interstellar medium, ISM) and the IGM, controls the competition between IGM inflow and galactic feedback processes, which in turn controls how the galaxy evolves (Faucher-Giguere & Oh 2023; Tumlinson et al. 2017).

Due to the low density of most of the gas in the CGM

(see for example, Zahedy et al. 2019), it is difficult to capture the physical processes taking place in the CGM using the emission from this gas. Diffuse Ly α emission is frequently detected from high- z (i.e., $z \geq 2$) galaxies which provide important information on the gas density and velocity field around galaxies (Wisotzki et al. 2018). However, such studies are rare for low- z , although there has been a steady attempt to map the CGM in Mg II emission either directly (Chisholm et al. 2020; Burchett et al. 2021) or in the stacked images (see for example, Dutta et al. 2023). As a result, absorption line spectroscopy remains the best means to understand the gas kinematics and physical processes that take place in the CGM. While the existence of large-scale gas flows (inflows/outflows) in the starforming galaxies is well-established by the “down-the-barrel” studies (Rubin et al. 2010, 2014; Tremonti et al. 2007), the distance of the flowing gas from the galaxy (which is crucial for deriving wind parameters such as mass outflow rate) cannot be precisely determined with respect to the stellar discs. In contrast, the projected distance of the absorbing gas from the host galaxy is well measured in CGM studies using bright background sources like galaxies and quasars. However, drawing a clear connection between star formation and gas absorption is challenging, particularly at large impact parameters.

* E-mail: labanya@iucaa.in (LKG)

† E-mail: anand@iucaa.in (RS)

‡ E-mail: petitjean@iap.fr (PPJ)

Historically Mg II doublet absorption seen in the spectra of quasars is used to trace the metal-enriched CGM around low- z galaxies (Bergeron & Boissé 1991). Probing the physical condition of the gas around galaxies using background quasar sight lines at very low impact parameters (e.g., within the regions influenced by winds over a characteristic time-scale of star formation) can provide vital clues on the role played by large-scale winds in shaping the physical conditions of the CGM and how it regulates galaxy evolution. For the past couple of years, we have been carrying out a systematic study of the CGM of $z \sim 0.7$ galaxies at low impact parameters by (i) searching for the host galaxies of Ultra-Strong Mg II absorbers (USMgII) and (ii) studying the nature of Mg II galaxies that happen to lie within very small impact parameters (i.e. Galaxies On Top of Quasars; GOTOQs) to background quasars (see Guha et al. 2022; Guha & Srianand 2023).

Here we concentrate on USMgII systems again. Following Nestor et al. (2007), we define the USMgII systems as the ones having the rest equivalent width of the Mg II $\lambda 2796$ line (W_{2796}) more than or equal to 3\AA . Given the canonical anti-correlation between W_{2796} and the impact parameter (D) for the general population of Mg II absorbers (Chen et al. 2010; Nielsen et al. 2013a), the impact parameters for the USMgII host galaxies are expected to be extremely low ($\lesssim 10$ kpc). The measured W_{2796} using low dispersion spectra is well known to be linked to the number of absorbing clouds and the velocity dispersion between them, rather than the column density (Petitjean & Bergeron 1990). For a fully saturated Mg II line a 3\AA limit on W_{2796} corresponds to a minimum velocity width of 320 km s^{-1} . Such large velocity spreads could be caused by (i) galactic-scale outflows (Nestor et al. 2011a), (ii) filamentary accretion onto galaxies (Rubin et al. 2012), and (iii) galaxy mergers (Rubin et al. 2010) and intra-group gas (Gauthier 2013; Nielsen et al. 2022; Zou et al. 2018). In such instances, one could use the measured metallicities (Lehner et al. 2013) and galaxy orientations relative to quasar sightlines to differentiate between the various possibilities (Kacprzak et al. 2012). To measure metallicity, one requires high-resolution spectra covering H I and metal absorption lines. For accurately measuring the orientation of host galaxies, one needs high spatial-resolution images.

In a previous paper (Guha et al. 2022), we studied the nature and environment of a well-defined sample of USMgII host galaxies at $z \sim 0.5$. We find that the impact parameters are larger than that predicted by the W_{2796} versus the D relationship of the general population of Mg II absorbers. The USMgII host galaxies seem to form a distinct population in the $W_{2796} - D$ plane. USMgII host galaxies are found to be massive and bright compared to those of the relatively weak Mg II absorption systems for the same impact parameters. At least 33% of the USMgII host galaxies (with a limiting magnitude of $m_r < 23.6$) are isolated, and the large W_{2796} in these cases may originate from gas flows (infall/outflow) in a single halo of a massive but not a starbursting galaxy. We also find galaxy interactions could be responsible for large velocity widths in at least 17% of the cases.

In the present study, we proceed further with a slightly higher redshift ($z \sim 0.7$) sample to identify any redshift evolution associated with these systems. This paper is organized as follows. In section 2, we discuss our USMgII sample at $z \sim 0.7$. Section 3 discusses the observations and data reduction procedures. In section 4, we describe the data anal-

ysis and the results from this survey. The discussions and summary & conclusions are provided in Section 5 and 6, respectively. Throughout this paper, we assume a flat Λ CDM cosmology with $H_0 = 70 \text{ km s}^{-1} \text{ Mpc}^{-1}$ and $\Omega_{m,0} = 0.3$.

2 THE USMgII SAMPLE AT $z \sim 0.7$

In this work we extend our study of USMgII absorbers (Guha et al. 2022, which focused on USMgII absorbers at $0.4 \leq z \leq 0.6$) to slightly higher redshifts. For this, we compiled a sample of USMgII absorption system candidates from the twelfth data release (DR12) of the Sloan Digital Sky Survey (SDSS, Alam et al. 2015; York et al. 2000) Fe II/ Mg II absorbers catalog (Zhu & Ménard 2013) that are accessible to the South African Large Telescope (SALT, Buckley et al. 2005) (i.e., with declination, $\delta \leq 10^\circ$) in the redshift range $0.6 \leq z_{abs} \leq 0.8$. Our preliminary search resulted in a total of 151 USMgII absorption system candidates along the line of sight towards 148 different background quasars. However, a careful visual inspection of the SDSS spectrum of each of these 151 USMgII absorption systems revealed that a total of 88 are basically C IV/ Si IV broad absorption lines (BAL) misidentified as USMgII systems. Additional 36 systems are wrongly identified as USMgII because of line blendings, poor SNR, or false identification of Mg II absorption doublets, leaving behind only 27 secure USMgII systems in the redshift range $0.6 \leq z_{abs} < 0.8$ with $\delta \leq 10^\circ$. Details of all these 151 absorption systems are provided in the appendix (Table A1 of Appendix A) where we explicitly mention whether the absorption system is a secure USMgII absorption system or falsely identified as a USMgII absorption system.

To confirm that the selected 27 USMgII systems are indeed bona fide USMgII absorption systems, we measure the rest equivalent widths of the Mg II $\lambda\lambda 2796, 2803$ absorption lines. For W_{2796} , we first approximate the continuum around the Mg II absorption lines with a smooth polynomial and then fit the absorption doublet using a pair of Gaussian profiles on top of this smooth polynomial. While fitting, we impose the redshift and velocity width of both the Gaussian profiles to be the same. This exercise confirms that within 1σ uncertainty all the selected 27 systems are indeed USMgII absorption systems. Similarly, we fit the associated Fe II $\lambda 2600$ and Mg I $\lambda 2853$ absorption lines each with a single Gaussian profile in addition to a smooth polynomial continuum, and compute their rest equivalent widths. Upon visual inspection of the fitted profiles for five of the USMgII systems (J0127–0550, J0150+0604, J0256+0110, J0908+0727, J0956+0018), even in the low-resolution SDSS spectra, we identify sub-structures in the absorption profiles of Mg II and Fe II. Subsequently, these absorption profiles are not very well characterized by a single Gaussian profile with velocity offsets between absorption components ranging from 100 to 300 km s^{-1} . The details of these 27 USMgII systems along the emission redshifts, absorption redshifts, and the obtained rest equivalent widths are given in Table 1. In the case of non-detections, we provide the 3σ upper limit on the REW.

Combining these findings for USMgII systems at $z = 0.6 - 0.8$ with that of Guha et al. (2022) for USMgII systems at $z = 0.4 - 0.6$ we can summarise that there are 260 USMgII candidates at $\delta < 10$ deg in the catalog of Zhu & Ménard

Table 1. Details of our USMgII sample. Columns (2), (3), and (4) respectively provide the quasar name, emission redshift (z_{qso}), and the absorption redshift (z_{abs}). Column (5) to (8) provides the REW of Mg II λ 2796, Mg II λ 2803, Fe II λ 2600, Mg I λ 2803 lines respectively.

No. (1)	Quasar (2)	z_{qso} (3)	z_{abs} (4)	W_{2796} (Å) (5)	W_{2803} (Å) (6)	W_{2600} (Å) (7)	W_{2853} (Å) (8)
1	J001030.81+012203.43	2.197	0.6433	3.19 ± 0.45	3.22 ± 0.46	2.01 ± 0.56	< 0.60
2	J002022.66+000231.98	2.749	0.7700	3.18 ± 0.28	3.03 ± 0.27	2.11 ± 0.37	0.87 ± 0.21
3	J002839.24+004103.05	2.493	0.6565	3.33 ± 0.19	3.29 ± 0.19	2.93 ± 0.19	1.21 ± 0.37
4	J003336.04+013851.06	2.658	0.7188	3.80 ± 0.30	3.11 ± 0.24	1.35 ± 0.10	0.42 ± 0.13
5	J005554.25-010058.62	2.363	0.7150	4.02 ± 0.67	3.80 ± 0.63	2.90 ± 0.89	1.74 ± 0.59
6	J010543.52+004003.86	1.078	0.6489	3.41 ± 0.21	2.87 ± 0.18	1.69 ± 0.17	< 0.48
7	J012711.11-055020.95	2.137	0.6838	3.19 ± 0.51	2.54 ± 0.40	3.52 ± 0.75	< 0.54
8	J014115.32-000500.98	2.130	0.6106	2.77 ± 0.38	2.02 ± 0.27	1.05 ± 0.28	< 0.42
9	J014258.83+094942.43	0.981	0.7858	3.90 ± 0.26	3.27 ± 0.22	2.43 ± 0.15	0.82 ± 0.17
10	J015007.91-003937.09	2.730	0.7749	4.34 ± 0.53	4.08 ± 0.50	3.04 ± 0.26	< 0.57
11	J015049.39+060432.42	2.676	0.6707	3.34 ± 0.22	2.69 ± 0.18	2.38 ± 0.28	0.77 ± 0.12
12	J025607.25+011038.56	1.3490	0.7255	3.29 ± 0.20	2.91 ± 0.18	2.29 ± 0.33	0.82 ± 0.12
13	J090805.76+072739.90	2.414	0.6123	5.30 ± 0.58	4.38 ± 0.48	4.24 ± 0.94	1.45 ± 0.30
14	J095619.49+001800.34	2.172	0.7820	6.34 ± 0.46	6.35 ± 0.46	5.43 ± 0.55	2.23 ± 0.51
15	J103325.92+012836.35	2.180	0.6709	3.11 ± 0.17	2.82 ± 0.15	1.53 ± 0.15	0.44 ± 0.08
16	J104642.70+045731.96	2.542	0.7849	4.47 ± 0.66	4.40 ± 0.65	2.19 ± 0.22	< 0.42
17	J111627.65+050049.96	2.571	0.7208	3.78 ± 0.48	3.47 ± 0.44	1.93 ± 0.27	< 0.41
18	J115026.11+090048.40	2.492	0.7568	3.39 ± 0.24	2.76 ± 0.19	1.66 ± 0.34	1.13 ± 0.11
19	J120139.57+071338.24	1.205	0.6842	4.55 ± 0.18	4.08 ± 0.16	2.30 ± 0.24	0.83 ± 0.11
20	J121727.80-011548.57	2.624	0.6642	4.02 ± 0.45	3.64 ± 0.41	2.88 ± 0.28	1.57 ± 0.44
21	J132200.79-010755.70	2.160	0.7226	3.24 ± 0.24	3.20 ± 0.24	3.05 ± 0.30	1.09 ± 0.14
22	J133653.73+092221.23	2.531	0.7059	3.06 ± 0.09	2.86 ± 0.08	2.03 ± 0.10	0.69 ± 0.08
23	J140017.69-014902.40	2.555	0.7928	4.23 ± 0.25	4.02 ± 0.24	3.45 ± 0.25	1.04 ± 0.34
24	J141930.09+034643.73	2.316	0.7250	3.30 ± 0.40	2.80 ± 0.34	1.52 ± 0.22	1.50 ± 0.40
25	J144936.18-011650.46	0.772	0.6620	3.66 ± 0.26	2.99 ± 0.21	1.37 ± 0.13	< 0.54
26	J145108.53-013833.06	2.390	0.7407	3.29 ± 0.25	2.96 ± 0.23	1.94 ± 0.31	< 0.62
27	J235639.31-040614.47	2.880	0.7707	3.77 ± 0.48	3.68 ± 0.47	1.81 ± 0.21	< 0.68

(2013) with $0.4 \leq z \leq 0.8$ and out of which we confirm only 54 of them to be secured USMgII absorbers.

3 SALT OBSERVATIONS AND DATA REDUCTION

To identify the galaxy or the galaxy group giving rise to the USMgII absorption along the quasar line of sights, we first identify all the galaxies from the Dark Energy Spectroscopic Instrument Legacy Imaging Survey (DESI-LIS, Dey et al. 2019, typically complete upto $m_r \leq 23.6$) within a projected distance of 100 kpc (at the photometric redshifts). Details of these galaxies are given in Table A2 of Appendix B. To optimize our spectroscopic identification process using long-slit spectroscopy, we mainly focus on the galaxies with photometric redshifts consistent within 1σ uncertainty with that of the USMgII systems and lying within 50 kpc from the quasar line-of-sight at the absorption redshift (as indicated by the dotted circles in Fig. 1). Next, we get the spectra of these candidate galaxies using the Southern African Large Telescope (SALT). In addition, whenever possible, we also observed potential galaxy candidates with impact parameters in the range 50–100 kpc.

The SALT spectroscopic observations were performed using the Robert Stobie Spectrograph (RSS, Burgh et al. 2003; Kobulnicky et al. 2003) in long-slit mode from June 2020 to February 2023 (Program IDs: 2020-1-SCI-010, 2020-2-SCI-019, 2021-1-SCI-006, 2021-2-SCI-012, 2022-1-SCI-016, 2022-

2-SCI-015). The slit orientation (quantified through the position angle (PA) used) for each USMgII system is suitably chosen such that all the candidate galaxies and quasars are observed simultaneously. For all our observations, we use the PG0900 grating along with a long slit-width of width $1.5''$ and the grating angles are so chosen that the expected nebular lines ([O II], [O III], and H β) from the USMgII host galaxies fall within the wavelength coverage of the spectrograph avoiding the CCD gaps. The details of the observations are provided in Table 2. Column (2) provides the names of the quasars observed. The date of observations, total exposure time, the position angle (PA) from the north, the grating angle, and the wavelength range covered are provided in the next five subsequent columns in that order.

The raw CCD frames obtained from the observations are first processed with the SALT data reduction pipelines (Crawford et al. 2010). Next, we use standard PyRAF (Science Software Branch at STScI 2012) routines to obtain the wavelength and flux-calibrated spectra of the quasars as well as the candidate galaxies. In summary, the science frames were first flat-field corrected, cosmic ray zapped, and then wavelength calibrated against a standard lamp spectrum. Next, we corrected the extinction due to the Earth's atmosphere, and then the 1D spectra of the quasar and the galaxy were extracted. These 1D spectra were then flux-calibrated against standard stars observed with the same settings as the quasar. Finally, we apply the air to vacuum wavelength transformation and correct for the heliocentric velocity.

Table 2. The observational log. Column (2) corresponds to the USMGR systems observed. The observations date, total exposure, the slit position angle from the north, the grating angle, and the wavelength range are provided in columns (3) - (7), respectively.

No.	Quasar	Date	Exposure (s)	PA (deg.)	Grating Angle (deg)	Wavelength Range (Å)
(1)	(2)	(3)	(4)	(5)	(6)	(7)
1	J002022.66+000231.98	2021-07-11	2400	17	20	6000 - 8985
		2021-08-03	2400	17	20	6000 - 8985
2	J002839.24+004103.05	2020-07-29	2560	124	18.125	5310 - 8320
		2020-09-15	2560	124	18.5	5450 - 8450
		2022-08-04	2560	67	18.125	5310 - 8320
3	J003336.04+013851.06	2020-06-24	2560	29	19.625	5870 - 8850
		2020-07-24	2560	29	19.25	5865 - 8865
		2021-07-16	2560	155	20	6000 - 8985
		2021-08-06	2280	155	20	6000 - 8985
4	J005554.25-010058.62	2021-08-10	2400	171	19.625	5870 - 8850
5	J010543.52+004003.86	2020-07-29	2560	141	18.5	5450 - 8450
		2020-10-13	2560	141	18.125	5310 - 8320
		2022-08-27	2560	106	18.5	5450 - 8450
6	J012711.11-055020.95	2020-07-01	2560	41	19.25	5865 - 8865
		2020-10-14	2560	41	18.875	5585 - 8585
		2022-08-20	2560	68	18.875	5585 - 8585
7	J014258.83+094942.43	2021-09-12	2200	86	20.375	6140 - 9120
		2021-08-04	2000	86	20	6000 - 8985
8	J015007.91-003937.09	2022-09-21	2560	0	20	6000 - 8985
9	J015049.39+060432.42	2020-10-16	2360	90	18.875	5585 - 8585
		2022-07-17	2360	90	18.5	5450 - 8450
		2022-09-23	2360	146	18.5	5450 - 8450
10	J025607.25+011038.56	2020-11-12	2580	133	20	6000 - 8985
		2021-08-09	2560	133	19.25	5865 - 8865
		2022-09-03	2560	95	19.25	5865 - 8865
		2021-08-10	2560	133	19.625	5870 - 8850
11	J090805.76+072739.90	2021-02-05	2300	73	18.875	5585 - 8585
		2021-02-06	2300	73	18.5	5450 - 8450
12	J095619.49+001800.34	2021-02-08	2580	135	20	6000 - 8985
		2021-04-07	2580	135	20.375	6410 - 9120
13	J103325.92+012836.35	2022-02-07	2440	21	18.875	5585 - 8585
14	J104642.70+045731.96	2021-04-14	2200	161	20.375	6140 - 9120
15	J111627.65+050049.96	2022-02-07	2300	87	19.625	5870 - 8850
16	J115026.11+090048.40	2022-02-06	2200	41	20	6000 - 8985
17	J120139.57+071338.24	2021-01-21	2300	149	19.25	5865 - 8865
		2021-04-12	2300	149	19.25	5865 - 8865
18	J121727.80-011548.57	2021-03-12	2580	139.25	19.25	5865 - 8865
		2023-01-23	2560	139	19.25	5865 - 8865
19	J132200.79-010755.70	2023-02-23	2560	132	19.625	5870 - 8850
		2023-02-24	2560	132	19.625	5870 - 8850
20	J133653.73+092221.23	2022-04-30	2200	162	19.625	5870 - 8850
		2023-02-22	2560	163	19.625	5870 - 8850
21	J140017.69-014902.40	2021-05-13	2560	0	20.375	6140 - 9120
		2021-06-13	2560	90	20.375	6140 - 9120
22	J141930.09+034643.73	2021-04-18	2300	142	20	6000 - 8985
		2021-05-17	2400	132	20	6000 - 8985
		2021-06-13	2400	67	20	6000 - 8985
23	J144936.18-011650.46	2020-06-16	2560	180	18.5	5450 - 8450
		2020-06-24	2560	180	18.875	5585 - 8585
24	J145108.53-013833.06	2020-07-22	2560	31	20	6000 - 8985
		2021-05-11	2560	61	19.625	5870 - 8850
25	J235639.31-040614.47	2017-06-05	2500	45	20.375	6140 - 9120
		2017-08-19	2350	315	20.375	6140 - 9120
		2020-09-08	2560	90	20	6000 - 8985

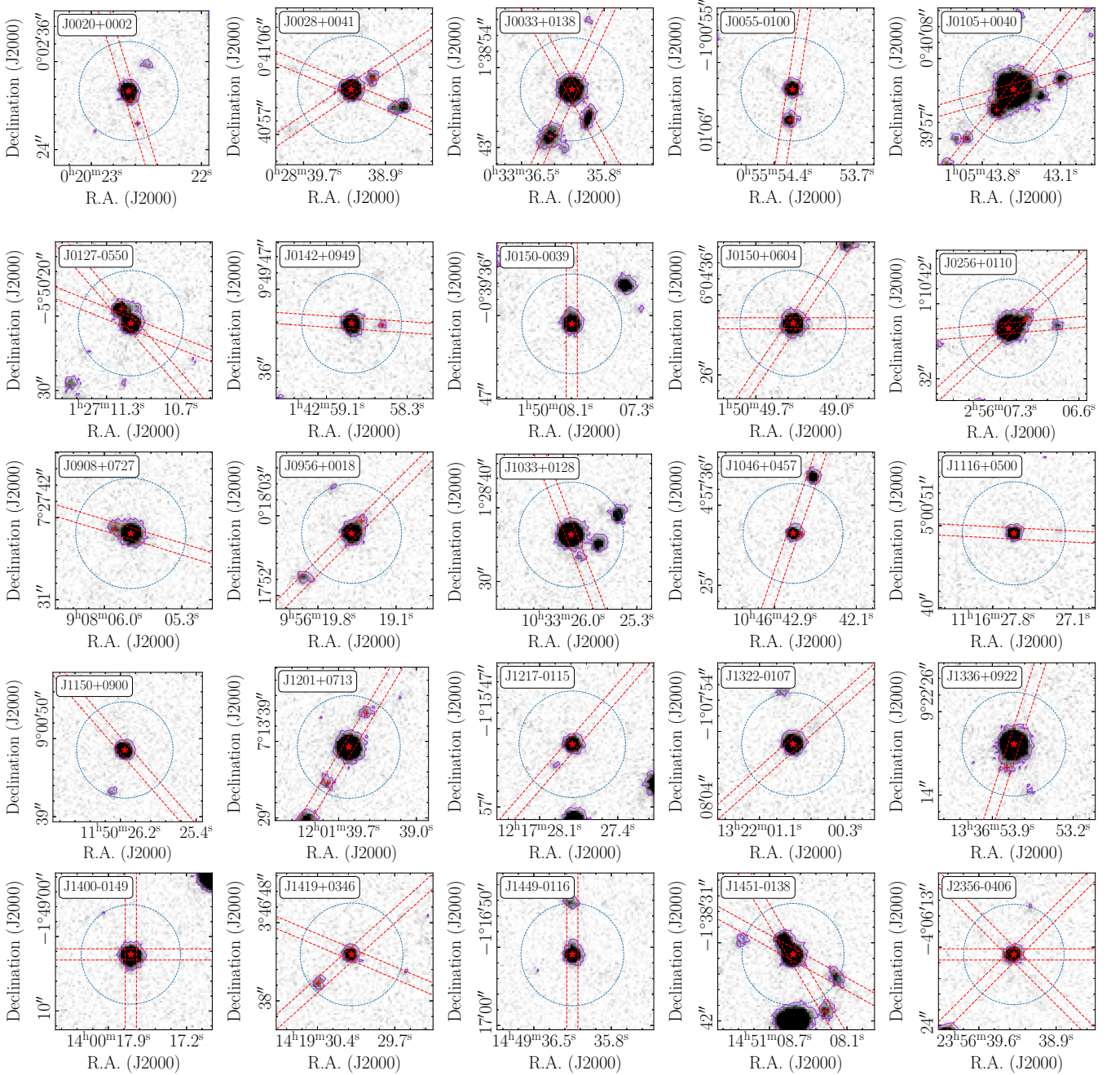


Figure 1. The DECaLS r-band images of the quasar fields with the quasar placed at the center and marked with a red ‘ \star ’. The slit configuration used is indicated with a pair of red dashed lines. The spectroscopically identified USMgII host galaxies are marked with a red ‘+’. The blue dashed circle in each panel corresponds to the circle of projected radius of 50 kpc at the absorption redshift.

4 ANALYSIS AND RESULTS

4.1 Identification of the USMgII host galaxies

Spectroscopic observations of host-galaxy candidates were completed using SALT for 25 of the 27 USMgII systems (i.e., excluding the USMgII absorbers along J0010+0122 and J0141–0005) in our sample. The r-band images of the fields together with the slit orientations (parallel dashed lines in red) used, and the 50 kpc impact parameter at the redshift of the absorber (indicated by the dashed circle) are shown in Figure 1. The spectroscopically confirmed USMgII host

galaxies are marked with a red ‘+’, and the quasar locations are marked with a red ‘ \star ’. As can be seen from this figure and Table A2 of the Appendix (in the online material), there are ten cases where we do not find any galaxy with $r < 23.6$ mag within an impact parameter of 50 kpc to the quasar sightline at the redshift of the USMgII system. These are, J0142+0949, J0150–0039, J0150+0604, J1046+0457, J1116+0500, J1217–0115, J1322–0107, J1400–0149, J1451–0138 and J2356–0406. The USMgII absorber towards J2356–0406 is a known GOTOQ (Joshi et al. 2017), and we obtained RSS spectra along three position angles to

No.	Quasar	Galaxy	z_{gal}	D (kpc)	$\log(M_*/M_\odot)$	M_B	[O II] Flux	SFR ($M_\odot yr^{-1}$)
(1)	(2)	(3)	(4)	(5)	(6)	(7)	(8)	(9)
1	J002022.66+000231.98	J002022.65+000230.68 J002022.58+000227.38	0.7684 0.7700	9.7 35.2	– $9.33^{+0.31}_{-0.24}$	– -19.08 ± 0.11	0.92 ± 0.18 0.71 ± 0.23	– (1.2) $1.04^{+0.88}_{-0.31}$ (1.0)
2	J002839.24+004103.05	J002839.05+004104.58	0.6565	22.2	$10.70^{+0.12}_{-0.13}$	-20.27 ± 0.09	0.94 ± 0.27	$11.56^{+10.80}_{-4.78}$ (0.3)
3	J003336.04+013851.06	J003336.24+013844.75	0.7178	50.3	$11.76^{+0.04}_{-0.06}$	-22.46 ± 0.07	1.88 ± 0.42	$56.90^{+11.65}_{-16.15}$ (2.0)
4	J005554.25–010058.62	J005554.28–010102.72 J005554.42–010115.20	0.7150 0.7161	29.8 120.7	$11.49^{+0.04}_{-0.05}$ $10.03^{+0.18}_{-0.17}$	-21.19 ± 0.07 -20.01 ± 0.10	< 1.06 0.80 ± 0.19	$4.72^{+5.31}_{-2.65}$ (< 0.4) $3.47^{+3.66}_{-2.00}$ (0.5)
5	J010543.52+004003.86	J010543.67+004001.10 J010543.97+003957.28	0.6490 0.6489	24.6 65.7	$10.35^{+0.11}_{-0.12}$ $9.54^{+0.14}_{-0.13}$	-20.90 ± 0.09 -20.14 ± 0.12	11.2 ± 1.0 0.81 ± 0.21	$5.57^{+2.93}_{-2.04}$ (3.2) $3.04^{+2.19}_{-0.99}$ (0.5)
6	J012711.11–055020.95	J012711.20–055019.01 J012711.91–055016.45	0.6829 0.6839	16.8 90.1	$10.48^{+0.16}_{-0.17}$ $10.77^{+0.11}_{-0.13}$	-21.35 ± 0.12 -20.90 ± 0.10	3.82 ± 0.87 1.73 ± 0.23	$7.93^{+5.71}_{-2.96}$ (2.6) $9.91^{+4.44}_{-2.94}$ (1.1)
7	J014258.83+094942.43	J014258.56+094942.20	0.7860	30.0	$12.01^{+0.13}_{-0.14}$	-21.68 ± 0.09	< 1.10	– (< 0.4)
8	J025607.25+011038.56	J025607.10+011039.80	0.7244	18.4	$11.04^{+0.14}_{-0.12}$	-21.26 ± 0.10	1.46 ± 0.28	$36.18^{+44.52}_{-16.68}$ (1.5)
9	J090805.76+072739.90	J090805.91+072740.58	0.6127	16.5	$10.73^{+0.13}_{-0.14}$	-20.57 ± 0.10	2.53 ± 0.33	$15.61^{+12.78}_{-7.19}$ (1.3)
10	J095619.49+001800.34	J095619.41+001802.00	0.7829	15.6	$10.72^{+0.14}_{-0.16}$	-21.06 ± 0.13	6.89 ± 0.52	$14.42^{+20.12}_{-7.00}$ (16)
11	J104642.70+045731.96*	J104642.62+045731.84	0.7848	8.9	–	–	0.88 ± 0.27	– (1.6)
12	J120139.57+071338.24	J120139.41+071342.84 J120139.77+071333.28	0.6854 0.6842	36.3 41.3	$10.98^{+0.14}_{-0.11}$ $11.42^{+0.13}_{-0.11}$	-21.43 ± 0.10 -21.50 ± 0.09	1.80 ± 0.37 2.91 ± 0.50	$42.97^{+45.06}_{-24.86}$ (1.2) $82.69^{+85.06}_{-24.86}$ (1.7)
13	J133653.73+092221.23	J133653.80+092217.96	0.7059	24.6	$10.47^{+0.16}_{-0.20}$	-20.47 ± 0.14	3.05 ± 0.30	$6.07^{+4.73}_{-2.10}$ (2.1)
14	J140017.69–014902.40*	–	0.7933	≤ 8	–	–	–	–
15	J141930.09+034643.73	J141930.39+034639.86	0.7252	42.8	$10.97^{+0.16}_{-0.17}$	-21.51 ± 0.12	8.0 ± 1.0	$23.29^{+17.46}_{-9.22}$ (2.7)
16	J144936.18–011650.46	J144936.20–011643.58	0.6618	48.1	$10.74^{+0.13}_{-0.08}$	-21.05 ± 0.10	4.73 ± 0.43	$21.06^{+56.17}_{-10.87}$ (3.0)
17	J145108.53–013833.06	J145108.24–013840.64	0.7414	64.1	$11.44^{+0.07}_{-0.10}$	-21.94 ± 0.08	1.00 ± 0.24	$34.44^{+9.42}_{-9.25}$ (3.5)
18	J235639.31–040614.47*	J235639.27–040413.80	0.7699	6.24	–	–	5.49 ± 0.43	– (3.9)

Table 3. Properties of the USMgII host galaxies. Columns (2) and (3) respectively indicate the quasars and corresponding USMgII host galaxies. Quasars marked with ‘*’ belong to the GOTOQs. Columns (4) and (5) provide the [O II] emission redshifts and the impact parameters of the host galaxies. Columns (6) and (7) provide the stellar masses and the rest frame absolute B band magnitude of the USMgII host galaxies, respectively. The [O II] fluxes are measured in the units of 10^{-17} ergs cm^{-2} s^{-1} and are provided in Column (8). Column (9) corresponds to the star formation rates based on SED fitting analysis. The values in the parenthesis correspond to the star formation rates based on the [O II] emission line luminosity. The typical errors associated are about one-third of the value.

find the location of the host galaxy using triangulation (see Figure C1 of Appendix C). In the case of J1046+0457 and J1400–0149, we detect [O II] emission at the correct redshift in the spectrum of the quasar. We thus confirm the USMgII host galaxies to be GOTOQs at low impact parameters (i.e., $D < 10$ kpc). In the case of J1046+0457, we identify the location of the galaxy from the extension seen in the DECaLS images (as discussed in Guha & Srianand 2023) and in the case of J1400–0149, we used the spectra obtained along two PAs.

In five cases (J0142+0949, J0150–0039, J1116+0500, J1217–0115, and J1322–0107), however, we do have a candidate galaxy within 50 kpc if we slightly relax our candidate galaxy selection criteria. Here, we consider the galaxies having photo- z consistent within $\sim 2\sigma$ uncertainty and allow them to be fainter than the limiting magnitude of $m_r = 23.6$. The impact parameter of the candidate galaxies ranges from $D \sim 10$ to 50 kpc. In these cases, slit PA is chosen to simultaneously observe the quasar and the galaxy candidate. In the case of J0142+0949, the targeted galaxy at $D \sim 30$ kpc ($z_{ph} \sim 0.9$) does not show any detectable nebular emission line in its spectrum. Still, we find a pair of absorption features consistent with the Ca II $\lambda\lambda 3935, 3970$ doublet at $z_{gal} = 0.786$ (see Figure B1 of Appendix B) and thus consistent with the redshift $z_{abs} = 0.7858$ of the USMgII system. Therefore, we consider this galaxy as the host galaxy of the USMgII absorber.

In the case of J1451–0138, we find a few galaxies with a projected distance of less than 50 kpc from the quasar. However, none has a photometric redshift consistent with the USMgII absorption redshift. We covered three galaxies in our observations (using two slit orientations) plus other galaxies outside the 50 kpc distance. We confirm only one galaxy with correct spectroscopic redshift but at an impact parameter of 64.1 kpc ($m_r = 21.59$). In the remaining three cases we do not detect [O II] emission from the galaxy candidates (typical 3σ limiting [O II] line flux of 7×10^{-18} ergs cm^{-2} s^{-1}). In the case of J0150+0604, no faint candidate galaxies are found within 50 kpc. We do not have any indication of a faint galaxy coinciding with the quasar image (i.e., GOTOQs) either in the available photometry or in our spectroscopic data.

In summary, out of the ten USMgII systems discussed above, we confirm three (J1046+0457, J1400–0149, and J2356–0406) of them to be GOTOQs. For J0142+0949 (even though the identified host galaxy has photo- z inconsistent within 1σ uncertainty) and J1451–0138 (impact parameter is larger than 50 kpc), we spectroscopically confirm the USMgII host galaxies. In four (J0150–0039, J1116+0500, and J1217–0115, and J1322–0107) cases, we have candidate galaxies (either faint or consistent photo- z within 2σ uncertainty) without spectroscopic confirmation. For J0150+0604, we do not have any candidate galaxy present within 50 kpc.

In nine cases (J0028+0041, J0033+0138, J0055–0100, J0127–0550, J0908+0727, J1150+0900, J1336+0922,

J1419+0346 and J1449–0116) we have only one galaxy with $r < 23.6$ mag with a consistent photometric redshift within 50 kpc. We could get spectra of 8 candidate galaxies (apart from the case of J1150+0900 where our SALT observation was not scheduled) and confirm their redshifts using nebular emission lines to be consistent with the corresponding USMgII system. Therefore, our target completeness is 89% for observations, and spectroscopic completeness is 100% for cases with only one candidate galaxy within 50 kpc of the USMgII absorbers.

In the remaining six cases, there are two galaxies within 50 kpc with consistent photometric redshifts. In three cases (J0105+0040, J0256+0110, and J1201+0713), we could get spectra of both galaxies. We confirm both (one of) the candidate galaxies to have consistent spectroscopic redshifts in the case of J1201+0713 (J0105+0040 and J0256+0110). In the case of J1033+0128, while we got the spectra of one of the candidates, we were unable to confirm the redshift using nebular emission lines. In the last two cases (J0020+0002 and J0956+0018), we could observe only one of the candidate galaxies (with the closest impact parameter) each and confirm them to have consistent spectroscopic redshifts. Therefore, the overall target completeness is 75% for observations, and spectroscopic completeness is 67% for cases with one candidate galaxy (brighter than 23.6 mag) within 50 kpc to the USMgII absorbers.

Among the 25 observed USMgII systems, we have successfully identified the USMgII host galaxies for 18 cases (16 based on [O II] emission and two based on Ca II absorption). The quasars (that show USMgII absorption systems) and the associated USMgII host galaxies are indicated in columns (2) and (3) of Table 3, respectively. Columns (4) and (5), respectively, provide the spectroscopic redshifts (z_{gal}) and the impact parameters (D). For four systems (J0020+0002, J0105+0040, J0127–0550, and J1201+0713), we could identify another galaxy within 100 kpc having spectroscopic redshift consistent with z_{abs} of the USMgII system. For the case of J0055–0100, we find an additional galaxy having consistent spectroscopic redshift with the USMgII absorption at an impact parameter of 120 kpc. Details of these additional galaxies are also provided in Table 3. Therefore, we confirm that at least in 5 out of 18 cases, the USMgII absorber could be associated with more than one galaxy having correct spectroscopic redshifts and impact parameters less than 125 kpc.

Finally, for all the spectroscopically confirmed redshifts, we compare the photometric redshift and spectroscopic redshift (see Figure C2 of Appendix C). We find that the two match well within 2σ uncertainty.

4.2 Properties of USMgII host galaxies

Having identified the host galaxies of USMgII absorbers, we estimate their properties, such as the stellar mass (M_*), rest frame absolute B band magnitude (M_B), and the ongoing star formation rate (SFR) using the available photometric and spectroscopic data and the spectral energy distribution (SED) modeling. As in Guha et al. (2022), we use the freely accessible Python tool Bayesian Analysis of Galaxies for Physical Inference and Parameter EStimation (Carnall et al. 2018, BAGPIPES). BAGPIPES takes into account Bruzual & Charlot (2003) stellar population models, which were built assuming the Kroupa & Boily (2002) initial mass

function (IMF) and most recently revised by Chevallard & Charlot (2016) to incorporate the MILES stellar spectrum library and an updated stellar evolutionary track (Marigo et al. 2013). The interstellar dust is assumed to follow Calzetti (1997) dust model.

During the fit, we keep the redshifts of the USMgII host galaxies fixed to their spectroscopic redshifts. Although BAGPIPES can simultaneously fit photometric and spectroscopic data, we only use the DESI-LIS three broadband photometric measurements to fit the SED as the SNR of individual pixels for the continuum regions in the spectra of most of the USMgII host galaxies is quite poor ($\text{SNR} < 3$). We also assume that all the stars in the galaxy have the same metallicity and use a flat prior in the range $0.01Z_\odot - 2.5Z_\odot$. We parameterize the star-formation histories with an exponential model (Carnall et al. 2019). We choose a uniform prior to the logarithm of the stellar mass in the range $0 \leq \log(M_*/M_\odot) \leq 13$. However, note that the parametric models impose strong priors on physical parameters and may bias the inferred galaxy properties. Although the stellar mass is less sensitive to such effects (typical offset of 0.1 dex from the true value), the offset for SFR can be as large as 0.3 dex (Carnall et al. 2019). The derived parameters for each galaxy are listed in Table 3.

Note galaxy properties could not be measured for four USMgII systems as their host galaxy image is blended with the quasar image. For the same reason, we could measure the galaxy parameters only for 26 out of the 36 nearest host galaxies in our combined USMgII sample. To enable easy comparison, we have also measured all these parameters for host galaxies in the MAGIICAT sample using the same technique (see Guha et al. 2022, for details).

4.2.1 [O II] Luminosity

As mentioned earlier, except for two cases, we detected [O II] nebular emission from USMgII host galaxies in our present sample. To obtain the spectroscopic redshifts, we fit the [O II] emission line using a pair of Gaussian functions having the same redshifts and velocity widths with the centroids of the two Gaussian functions separated by the ratio of the rest wavelengths of the [O II] $\lambda\lambda 3729, 3727$ lines. While fitting, the amplitude ratio of these two Gaussian functions is allowed to vary between 0.3 to 1.5 (Osterbrock & Ferland 2006). In principle, this flux ratio can be used to constrain the electron density. However, due to the poor velocity resolution of the SALT spectra, the uncertainty in this ratio is large, which prevents us from constraining the electron density accurately.

The [O II] line fluxes (combined flux of the doublet) obtained from simple integration over the line profile are given in column (8) of Table 3. The [O II] nebular line fluxes are then converted to the [O II] line luminosities ($L_{[\text{O II}]}$) based on their redshifts and the assumed background cosmology. Note that the measurements of [O II] luminosity are affected by two factors – the slit-loss and the dust attenuation. To correct for the slit-loss, we assume that the slit-loss is independent of the observed wavelength. Thus, we scale the observed spectra to match the synthetic spectra obtained from the SED fitting of available photometric points using the least square minimization method. We then multiply this scale factor with $L_{[\text{O II}]}$ to correct for the slit-loss. However, to estimate the dust content in these galaxies, we would need either at least two H I Balmer lines in emission or good-quality continuum spectra

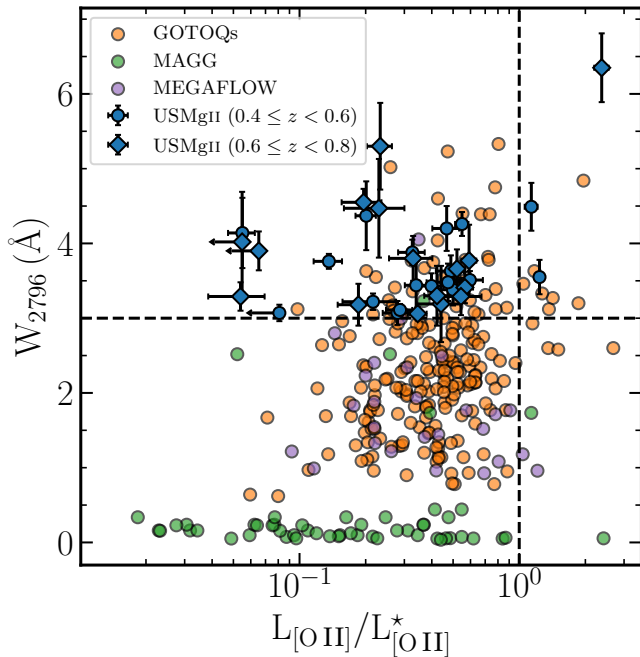


Figure 2. Scatter plot of W_{2796} against the [O II] line luminosity ($L_{[\text{O II}]}$) of the associated Mg II host galaxies. To correct for redshift evolution, we have scaled the $L_{[\text{O II}]}$ according to the characteristic [O II] line luminosity ($L_{[\text{O II}]}^*$) at that redshift. The orange, green, purple, and blue points (diamond/circle) correspond to the Mg II host galaxies from the GOTOQs (Joshi et al. 2017), MAGG survey (Dutta et al. 2020), MEGAFLOW survey (Schroetter et al. 2019), and the USMgII host galaxies (high redshift / low redshift), respectively. The horizontal and vertical black dashed lines correspond to the W_{2796}^{cut} of USMgII host galaxies and $L_{[\text{O II}]}^*$ galaxies, respectively.

of these galaxies with sufficient SNR. As for all the cases, we have neither, so we do not correct for dust attenuation.

In Figure 2, we show the scatter plot of W_{2796} versus the $L_{[\text{O II}]}$ of the associated Mg II host galaxies. To account for the redshift evolution, we have scaled the $L_{[\text{O II}]}$ with respect to the characteristics [O II] line luminosities ($L_{[\text{O II}]}^*$, Comparat et al. 2016) at the host galaxy redshifts. The orange, green, purple, and blue points correspond to the Mg II host galaxies from the GOTOQs (Joshi et al. 2017), MAGG survey (Dutta et al. 2020), MEGAFLOW survey (Schroetter et al. 2019), and the USMgII host galaxies, respectively. The $L_{[\text{O II}]}$ for the USMgII host galaxies varies from $0.05L_{[\text{O II}]}^*$ to $2.37L_{[\text{O II}]}^*$ with a median value of $0.37L_{[\text{O II}]}^*$. Using the lowest [O II] line luminosity as the detection threshold (i.e., $L_{\text{min}} = 0.05L_{[\text{O II}]}^*$) and the [O II] line luminosity function (Comparat et al. 2016) at $z \sim 0.6$, we find that the total number of expected super- $L_{[\text{O II}]}^*$ galaxies for a random population of galaxies are only about 3% implying only one super- $L_{[\text{O II}]}^*$ galaxies among the detected USMgII host galaxies. The expected median line luminosity for the random population of galaxies (at $z \sim 0.6$) is $\sim 0.1L_{[\text{O II}]}^*$. For our USMgII sample, however, we have three super- $L_{[\text{O II}]}^*$ galaxies and the median line luminosity ($0.37L_{[\text{O II}]}^*$) is also significantly high, even without correcting for dust extinction.

Out of all the GOTOQs, only $\sim 5\%$ are super- $L_{[\text{O II}]}^*$ galaxies. If we restrict ourselves to GOTOQs that produce USMgII

absorption, we find $\sim 15\%$ of them are super- $L_{[\text{O II}]}^*$. Like the USMgII galaxies, the [O II] luminosities of GOTOQs should be taken as lower limits as they are not corrected for fiber loss and dust extinction. For the MEGAFLOW sample, out of 26 Mg II host galaxies, only two ($\sim 8\%$) are super- $L_{[\text{O II}]}^*$ galaxies. Among the 53 galaxies associated with Mg II absorption in the MAGG sample, only two ($\sim 4\%$) are super- $L_{[\text{O II}]}^*$ galaxies. In the above two samples, there are only three USMgII systems, and none of them are found to be a super- $L_{[\text{O II}]}^*$ galaxy. Therefore, when we combine all the USMgII absorbers in different samples, we find $\sim 12 \pm 4\%$ of the host galaxies have super- $L_{[\text{O II}]}^*$. This, together with the high mean luminosity found above, confirms the early finding of Guha et al. (2022) that USMgII absorbers are preferentially hosted by galaxies having higher- $L_{[\text{O II}]}$ compared to field galaxies.

A Spearman rank correlation analysis between W_{2796} and $L_{[\text{O II}]}^*/L_{[\text{O II}]}$ yields a significant correlation between these two quantities ($r_S = 0.28$ and p -value $\sim 10^{-7}$), which is also reported in literature (Ménard et al. 2011; Joshi et al. 2018). However, this correlation is driven by weak Mg II absorbers. The correlation gets weaker as we restrict ourselves to the stronger Mg II absorbers (see Guha et al. 2022, for details). For example, for $W_{2796} > 1\text{Å}$, Spearman rank correlation analysis gives $r_S = 0.16$ and p -value = 0.008, while for $W_{2796} > 2\text{Å}$, we get $r_S = 0.05$ and p -value = 0.52. It is also clear from Figure 2 that there is no clear trend among the USMgII absorbers between W_{2796} and $L_{[\text{O II}]}$.

Next, we look for any redshift evolution in the [O II] luminosity of USMgII host galaxies over the redshift range $0.4 \leq z \leq 0.8$. We do not find any redshift evolution in the [O II] luminosities of the USMgII host galaxies with a Spearman correlation coefficient $r_s = 0.07$ with p value of 0.68. This is contrary to the mild evolution shown by $L_{[\text{O II}]}^*$ over the same redshift range (Comparat et al. 2016). It will be useful to confirm this with better-quality spectra after applying appropriate dust corrections.

4.2.2 Star formation rates

Next, we consider the current star formation rates (SFR) of the USMgII host galaxies. We measure the star formation rates using two different methods. The first method is based on the [O II] nebular line luminosity (Kennicutt 1998, given inside the brackets in the last column of Table 3), and the second method is based on the SED fitting (last column of Table 3). The SFR obtained using the [O II] emission line has systematic uncertainties that depend on variation in reddening, chemical abundance (stellar mass through the mass metallicity relations), and ionization (Moustakas et al. 2006; Gilbank et al. 2010). The inferred SFR using [O II] nebular emission is less than measured using SED fitting and as in Guha et al. (2022), for the reasons mentioned above, we use the SFR measurements based on SED fitting in our analysis.

We find a mild redshift evolution of the SFR of the USMgII host galaxies, obtained using SED fitting, over the redshift range $0.4 \leq z \leq 0.8$. The Spearman correlation coefficient between the SFR and z , $r_s = 0.61$, with p value being ~ 0.001 . Since our host galaxy sample is magnitude limited some of the redshift evolution may be biased by this. In Figure 3, we show the scatter plot between the ongoing star formation rates obtained from the SED fitting scaled by the star for-

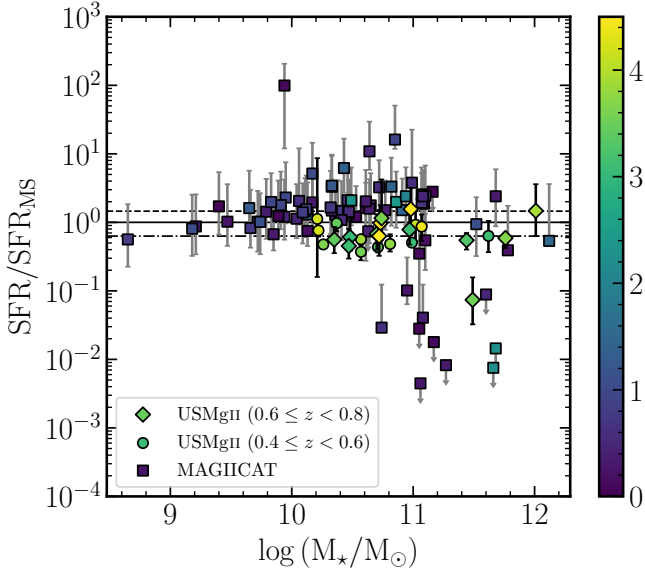


Figure 3. Scatter plot of the ongoing star formation rates (SFR) scaled by the star formation rate of a main sequence galaxy (SFR_{MS}) of the same mass at the same redshift, color-coded as W_{2796} against the stellar masses of the MgII absorbers. The diamond, circle, and square markers correspond to the high redshift USMgII host galaxies, low redshift USMgII host galaxies, and the MAGIICAT host galaxies, respectively. The solid black line corresponds to the main sequence SFR. The dotted and the dash-dotted line correspond to the median SFR of MAGIICAT and USMgII host galaxies, respectively.

mation rate of a main sequence galaxy (SFR_{MS}) of the same mass at the same redshift (Speagle et al. 2014), against their stellar masses. We scale the SFR with the main sequence SFR to account for redshift evolution. The points are color-coded by W_{2796} . The solid black line corresponds to the main sequence SFR. The dotted and the dash-dotted line correspond to the median SFR of MAGIICAT and USMgII host galaxies, respectively. The new data added from this work confirms that the USMgII host galaxies are not starburst galaxies and have star formation rates slightly lower than that expected for the main-sequence galaxies (Guha et al. 2022). However, note that the star formation rates are obtained from SED fittings based on the multiband galaxy photometries without the galaxy spectra can have large offsets (up to a factor 2) and can at best be main sequence galaxies.

4.3 W_{2796} versus impact parameter

In this section, we revisit the well-known anti-correlation between W_{2796} and impact parameter (Bergeron & Boissé 1991; Steidel 1995; Chen et al. 2010; Nielsen et al. 2013a) for the MgII absorbers. In particular, we are interested in (i) understanding this relation for USMgII absorbers by combining the present data with those from Guha et al. (2022) and (ii) how the global fit for the MgII systems gets modified by the inclusion of USMgII absorbers that mostly populate the low D - high W_{2796} region of the $W_{2796} - D$ plane. For consistency and simplicity, we consider the host galaxy as the one with the smallest impact parameter in any of the samples used

here when there is more than one galaxy identified at the correct redshift.

In the left panel of Figure 4, we show the points from our USMgII sample, GOTOQs from Guha & Srianand (2023), and additional measurements from different samples from the literature. The red points (circles for galaxies from Guha et al. (2022) and squares for galaxies from this work) correspond to the USMgII host galaxies from our observations. The orange, blue, violet, gray, brown, green, and pink circular points correspond to the isolated galaxies in Guha & Srianand (2023), MAGIICAT survey (Nielsen et al. 2013a), Huang et al. (2021), MAGG survey (Dutta et al. 2020), Kacprzak et al. (2013), DLAs and sub-DLAs (Rahmani et al. 2016), and Rubin et al. (2018) respectively. For DLAs and sub-DLAs, we obtained the W_{2796} from measurements available in the literature and used the impact parameters quoted in Rahmani et al. (2016). It is good to recollect that the W_{2796} measurements reported in Rubin et al. (2018) are towards background galaxies, unlike all other measurements towards quasars. We found some of the MgII systems in the literature sample are observed in two different surveys, and we made sure that the individual points plotted in Figure 4 and used for our statistical analysis correspond to a unique MgII system by removing the duplicates.

4.3.1 Relationship for the USMgII systems

First, we study the $W_{2796} - D$ distribution of USMgII systems (see Figure 5). The top part of Figure 5 shows the distribution of impact parameters for USMgII systems. The impact parameter of the USMgII host galaxies in the present sample varies from 6.24 to 64.1 kpc with a median of 23 kpc. Points in this plot are color-coded by their absorption redshifts. The red squares (circles) correspond to our measurements for high- z (low- z) USMgII systems, whereas those from the literature (from Dutta et al. 2020; Bouché et al. 2007; Schroetter et al. 2015; Nestor et al. 2011b) are shown with circles of different colors. For the combined USMgII sample, the impact parameter ranges from 6.24 kpc to 79 kpc with a median of 19 kpc. As noted by Guha et al. (2022), the USMgII systems do not follow the $W_{2796} - D$ anti-correlation. The Spearman correlation test yields no significant correlation ($r_s = 0.12$, $p = 0.40$) between these two quantities.

It is well known that the $W_{2796} - D$ relationship has a large scatter, and absorbers of a given rest equivalent width can originate from a wide range of impact parameters. Since our sample is based on large W_{2796} cutoff (i.e. $W_{2796}^{cut} = 3\text{\AA}$), it is important to check how the imposed W_{2796}^{cut} influences the measured correlation. To explore this, we measure the Spearman rank correlation coefficient r_s between W_{2796} and D for different values of W_{2796}^{cut} for the full sample. We notice that the strength of the anti-correlation between the W_{2796} and D becomes statistically insignificant if we confine ourselves to the stronger W_{2796} , i.e., $W_{2796}^{cut} \geq 1.5\text{\AA}$ (see Figure 6). For higher values of W_{2796}^{cut} , the data suggests a positive correlation coefficient but with less statistical significance. This demonstrates that when host galaxies are studied for an absorber-centric sample, the derived relationship between W_{2796} and D will be very sensitive to the W_{2796} cut-off used. Recently DeFelippis et al. (2021) discussed the W_{2796} vs. D relationship in their cosmological hydrodynamical simulations (see their figure 4). While high W_{2796} absorption are

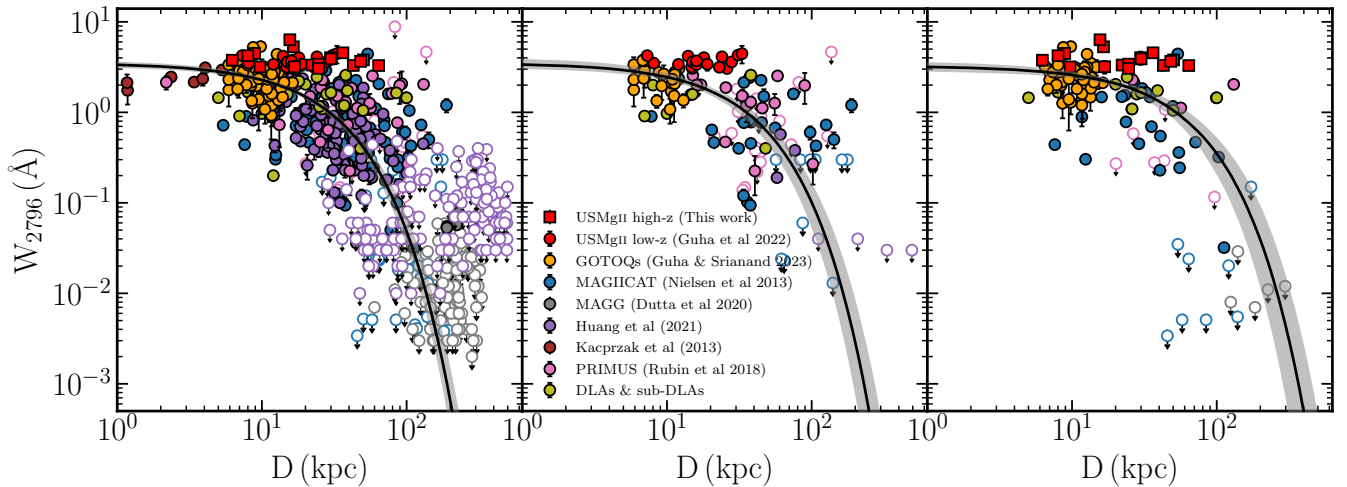


Figure 4. The *left panel* shows the impact parameter (D) versus the W_{2796} anti-correlation over the full redshift range for the isolated galaxies. The red squares correspond to the high-redshift USMgII absorption systems. The red (circle), orange, blue, violet, gray, brown, green, and pink points are taken from the low redshift USMgII survey (Guha et al. 2022), GOTOQs (Guha & Srianand 2023), MAGIICAT survey (Nielsen et al. 2013a), Huang et al. (2021), MAGG survey (Dutta et al. 2020), Kacprzak et al. (2013), DLAs and sub-DLAs, and Rubin et al. (2018) respectively. The solid black line corresponds to the best-fit log-linear model, and the shaded region corresponds to the 1σ errors associated with it. The *middle* and *right panel* show the same, but only for the redshift ranges, $0.4 \leq z_{abs} < 0.6$, and $0.6 \leq z_{abs} < 0.9$ respectively.

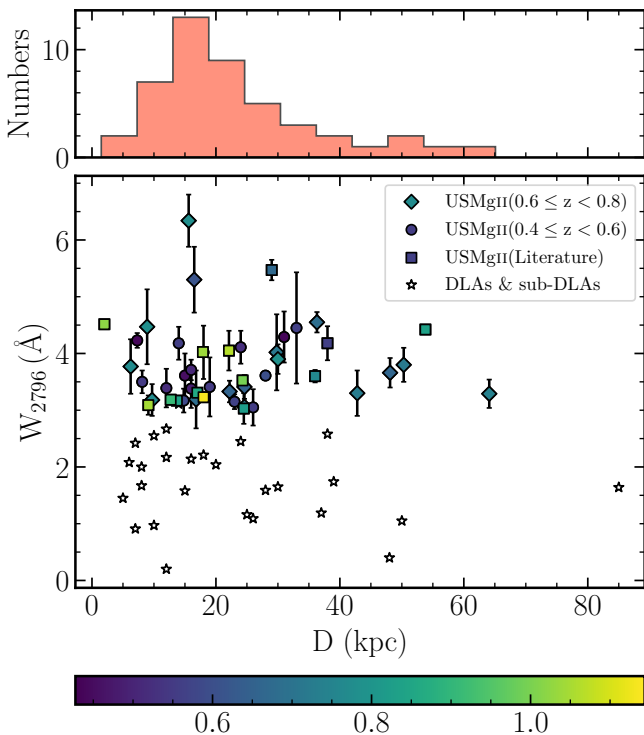


Figure 5. W_{2796} vs the impact parameters (D) for the USMgII host galaxies color coded by their absorption redshifts. The diamonds (circles) indicate our measurements for $0.4 \lesssim z \lesssim 0.6$ ($0.6 \lesssim z \lesssim 0.9$) USMgII sample. Squares show the data from the existing literature. The open stars are for the DLAs and sub-DLAs in the redshift range $0.4 \lesssim z \lesssim 1.0$ (Rahmani et al. 2016). The top panels show the distribution of impact parameters for the USMgII absorbers.

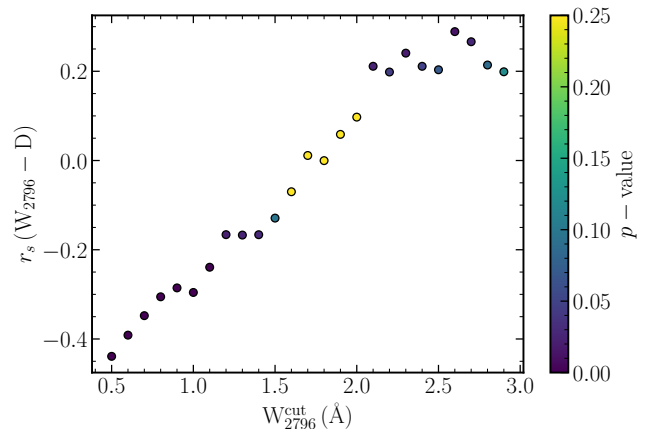


Figure 6. The Spearman rank correlation coefficient between the W_{2796} and D for a given W_{2796}^{cut} color-coded according to the p values with the null hypothesis that these two datasets are uncorrelated. For a small W_{2796}^{cut} , there is a significant anti-correlation between W_{2796} and D . However, as W_{2796}^{cut} increases, the significance of the anti-correlation keeps on decreasing and completely vanishes for W_{2796}^{cut} of 1.5 \AA .

not well represented in their simulations, there is also a lack of correlation between W_{2796} and D for strong Mg II absorber (defined as $W_{2796} > 0.5 \text{ \AA}$) along selected sightlines. On the other hand, for sightlines generated around halos, the anti-correlation is seen with a large scatter. Our findings align with these results even though the simulated W_{2796} are much weaker than that of USMgII systems.

It is known that galaxy properties like M_* , M_B , and the star formation rate may introduce scatter in the W_{2796} vs. D relationship. In the following sections, we will explore whether the large scatter in D is related to the scatter in the galaxy properties. Alternatively, the lack of correlation

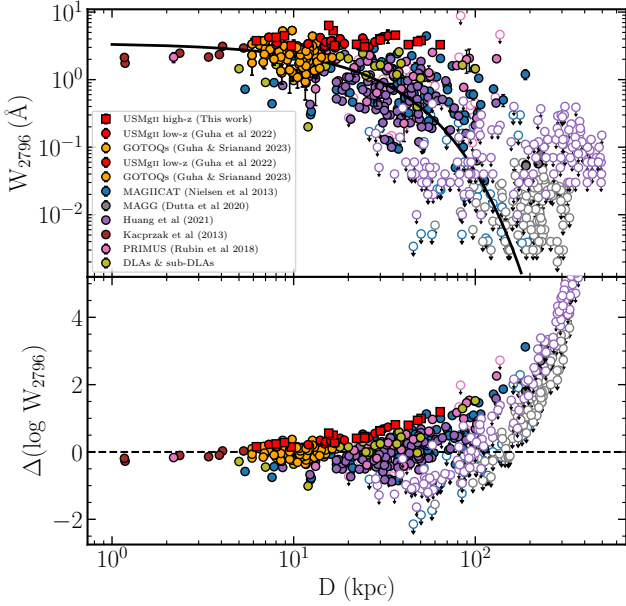


Figure 7. The scatter in the $W_{2796} - D$ anti-correlations. The top panel shows various Mg II absorption systems in the $W_{2796} - D$ space from this work and the literature. The solid black line represents the best-fit log-linear curve. This plot is the same as the left panel of Figure 4. The bottom panel shows the difference between the observed $\log(W_{2796})$ and the best-fit model for that impact parameter.

between W_{2796} and D could be related to a good fraction of USMgII absorbers not originating from the CGM around a single galaxy but contributed by several galaxies. Below we will discuss this possibility as well.

4.3.2 Redshift evolution

Here, we study the possible redshift evolution of the $W_{2796} - D$ relationship for the full Mg II absorber population. The solid black line in Figure 4 corresponds to the best-fit log-linear model, and the shaded region corresponds to the 1σ error associated with it. The maximum likelihood fitting prescription we use, including the upper limits, is provided in Guha et al. (2022). The middle and right panels show the same, but for the redshift ranges, $0.4 \leq z_{abs} < 0.6$, and $0.6 \leq z_{abs} \leq 0.9$ respectively. The best-fitted parameters for the full sample and systems in two redshift ranges are given in Table 4. The quoted values of σ in Table 4 are larger than most of the literature values. In the bottom panel of Figure 7, we show the residual of \log of equivalent width (i.e., observed $\log W_{2796}$ minus the predicted value from our best fit) as a function of impact parameter. It is evident that USMgII points form the upper envelope of the scatter, and the scatter increases as we go towards higher D .

We attribute the large scatter around the best-fit relation to the lack of correlation between W_{2796} and D found for the USMgII systems and the large scatter in W_{2796} at the low- D found for GOTOQs. As described in Guha & Srianand (2023) the inclusion of data at low impact parameters has increased the value of β compared to what has been reported in the literature. For the combined sample, our best fit param-

Redshift	α	β	σ
$0 < z < 1.5$	-0.019 ± 0.002	0.540 ± 0.028	1.09 ± 0.05
$0.4 \leq z < 0.6$	-0.015 ± 0.003	0.538 ± 0.045	1.13 ± 0.10
$0.6 \leq z \leq 0.9$	-0.010 ± 0.002	0.514 ± 0.044	1.29 ± 0.10

Table 4. Best fitting parameters for the log-linear characterization of the W_{2796} vs D anti-correlations for different redshift ranges.

eters suggest $W_{2796}(D=0) \sim 3.5 \text{ \AA}$ and characteristic impact parameter scale (i.e. $-1/(2.303 \times \alpha)$) is ~ 23 kpc.

Neither α nor β shows any significant change between the two distinct redshift ranges considered here. In addition, the KS-test confirms the W_{2796} distribution in these two redshift bins is not significantly different (p-value of 0.06). To avoid any bias introduced by differences in the W_{2796} distribution, we considered several sub-sample by matching the distribution of W_{2796} and confirming the lack of any significant redshift evolution in both α and β . For ease of viewing, in Figure 8, we plot the best-fit relations and associated errors for the two redshift ranges. As mentioned, $W_{2796}(D=0)$ does not evolve with redshift. Even though there is no significant difference between the best-fitted values of α , the plot suggests a slight excess in W_{2796} at large D for the high- z sub-sample.

Lundgren et al. (2021) have reported $\alpha = -0.008 \pm 0.001$ and $\beta = 0.51 \pm 0.03$ for $z > 1$ using their data combined with the available data from the literature (from Bouché et al. 2012; Lundgren et al. 2012, 2021; Schroetter et al. 2019). The β value they obtained is consistent with what we report in Table 4. The α value quoted by Lundgren et al. (2021) is slightly low but consistent within 2.3σ with our measurements in two low- z bins. By comparing their values of α and β with those of Nielsen et al. (2013a) (i.e., $\alpha = -0.015 \pm 0.002$ and $\beta = 0.27 \pm 0.11$) Lundgren et al. (2021) suggested a possible evolution in the gas distribution around galaxies at $z \sim 0.4$ and $z \sim 1.5$. To ensure that our result is not dominated by any bias arising from differences in the W_{2796} distribution, we have measured α and β of 500 random sub-samples from our sample that have the same number of absorbers having the distribution of W_{2796} similar to that of the sample of Lundgren et al. (2021). Using the log-linear fits of these realizations, we obtain $\alpha = -0.011 \pm 0.001$ and $\beta = 0.48_{-0.01}^{+0.02}$. This again confirms the lack of strong redshift evolution in α and β . In Figure 8, we also show the best-fit relationship for the high- z sample of Lundgren et al. (2021). As before, we notice that at large impact parameters, the best fits suggest higher W_{2796} at high- z . This figure also suggests no significant redshift evolution in the W_{2796} vs. D relationship at $D < 20$ kpc.

Dutta et al. (2020) have obtained $\beta = -0.05_{-0.38}^{+0.42}$ and $\alpha = -0.010 \pm 0.003$ for closest galaxies at $z \sim 0.8-1.5$ to the line of sight to 28 background quasars. Their α values are consistent with our values. However, the inferred $W_{2796}(D=0)$ value is lower than ours, albeit with large errors. This is related to the poor representation of galaxies with low impact parameters (i.e., $D < 20$ kpc) in their sample.

How the $W_{2796} - D$ relationship evolves with z has an important consequence on the redshift evolution of the number of Mg II absorbers per unit redshift path length (i.e., dN/dz). For absorbers with $W_{2796} > 1 \text{ \AA}$, $dN/dz = 0.16, 0.20$ and 0.31

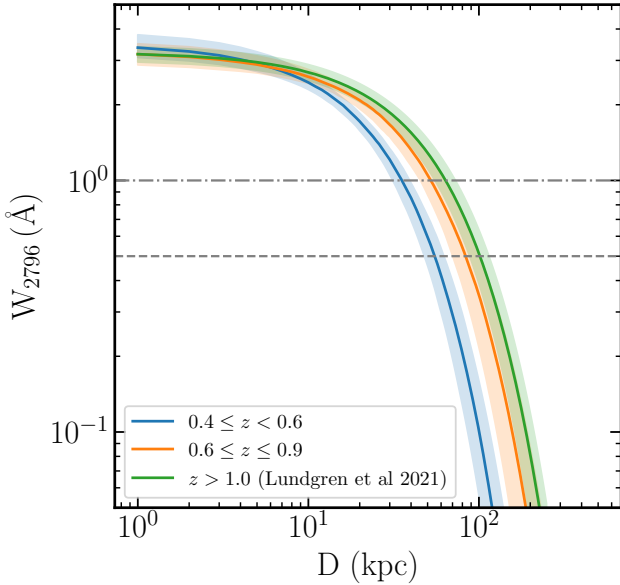


Figure 8. Redshift evolution of the $W_{2796} - D$ anti-correlation. The blue and orange lines correspond to the best fit $W_{2796} - D$ curve for the redshift range $0.4 \leq z < 0.6$ and $0.6 \leq z \leq 0.8$, respectively. The green curve is taken from [Lundgren et al. \(2021\)](#) and corresponds to the best fit $W_{2796} - D$ anti-correlation for the redshift range $z \geq 1.0$. The grey dot-dashed and dashed horizontal lines correspond to $W_{2796} = 1\text{\AA}$ and $W_{2796} = 0.5\text{\AA}$ respectively.

for $z = 0.5, 0.7$ and 1.3 respectively ([Zhu & Ménard 2013](#)). When we consider $W_{2796} > 0.5\text{\AA}$, the corresponding values are 0.41, 0.47, and 0.62. Thus systems with the largest equivalent width tend to show a slightly more rapid increase with redshift compared to those with the lowest equivalent width. In a simple model where all known galaxies have a spherical gaseous halo of the same radius and gas covering factor f_c , the average number of Mg II absorbers per unit redshift interval is given by $\langle dN/dz \rangle = f_c \pi D_{max}^2 \int_{L_{min}}^{\infty} \phi(L, z) dL \times dl/dz$. Here, D_{max} is the maximum impact parameter for a given value of W_{2796}^{cut} for which dN/dz is computed. $\phi(L, z)$ is the galaxy luminosity function at redshift z , and dl/dz is the differential comoving path length per unit redshift interval.

From [Faber et al. \(2007\)](#) we find the average number density of galaxies (with $-30 \leq M_B \leq -10$ and $M_B^* \sim -21.3$) per unit physical volume is ~ 0.90 and $\sim 1.74 \text{ Mpc}^{-3}$ at $z = 0.5$ and 1.1 respectively. Thus a factor of 2 change in dN/dz over the redshift range $0.5 \leq z \leq 1.1$ can purely originate from the redshift evolution of the galaxy luminosity function. From Figure 8, if the covering fraction is independent of D , then the number density of low W_{2796} is expected to show stronger redshift evolution. This is contrary to the observed results quoted above. Thus one requires the covering fraction to change with D . This expectation is consistent with the finding of [Lan \(2020\)](#). Their results suggest that over the redshift range $0.5 \leq z \leq 1.1$, the covering fraction of star-forming galaxies ($M_* \sim 10^{10} M_{\odot}$) associated with strong Mg II absorption ($W_{2796} \geq 1\text{\AA}$) increases from 0.19 to 0.41, implying an increase of the covering fraction by a factor of ~ 2 . The same for weak absorbers ($W_{2796} < 1\text{\AA}$) changes from 0.15 to 0.24, implying an increase by a factor of ~ 1.5 .

4.3.3 Dependence on stellar mass

[Churchill et al. \(2013a\)](#) have noted that for a given W_{2796} , the host galaxies at high impact parameters tend to have larger halo masses. This section investigates the presence of such a trend in our USMgII sample. In column 6 of Table 3, we provide the present sample's stellar masses of the USMgII host galaxies. The stellar mass of the USMgII host galaxies at $z \sim 0.7$ ranges from $10.35 \leq \log(M_*/M_{\odot}) \leq 12.01$ with a median value of 10.86. In the combined sample of USMgII host galaxies, the stellar mass ranges from $10.21 \leq \log(M_*/M_{\odot}) \leq 12.01$ with the median of $\log(M_*/M_{\odot}) = 10.73$. We find a mild evolution in the stellar masses of the USMgII host galaxies over the redshift range $0.4 \leq z \leq 0.8$ (Spearman correlation coefficient, $r_s = 0.48$ with p value of 0.01). As mentioned before, some redshift evolution may be influenced by the fact that we are using a magnitude-limited sample. For the MAGIICAT host galaxies, the stellar masses are found to be in the range $8.65 \leq \log(M_*/M_{\odot}) \leq 12.12$ with a median value of 10.51. Even though the two samples overlap in M_* ranges, the USMgII host galaxies tend to have higher M_* values as suggested by the median values.

In the left panel of Figure 9, we show the scatter plot of M_* versus D for host galaxies of the general Mg II system population from the MAGIICAT sample and USMgII systems in our sample color-coded according to the W_{2796} . For the MAGIICAT host galaxies, we also find a correlation between M_* and D , which can be characterized by a linear fit of the form $\log(M_*/M_{\odot}) = (0.036 \pm 0.006)D (\text{kpc}) + (9.301 \pm 0.225)$ (see [Guha et al. 2022](#)). The solid black straight line corresponds to this fit, and the grey region to the 1σ uncertainty to the fit. This aligns with the findings of [Churchill et al. \(2013b\)](#); [Rubin et al. \(2018\)](#); [Huang et al. \(2021\)](#), who reported that massive galaxies produce stronger absorption for a similar impact parameter. Considering the USMgII host galaxies alone, we find a possible mild correlation between M_* and D . A Spearman rank correlation analysis returns a correlation coefficient of $r_s = 0.5$ and a p -value of 0.009. A linear fit to the data for the USMgII galaxies gives $\log(M_*/M_{\odot}) = (0.019 \pm 0.007)D (\text{kpc}) + (10.341 \pm 0.203)$. The solid blue line in the left panel of Figure 9 corresponds to this fit. For a given impact parameter, the stellar mass of host galaxies of USMgII absorbers is systematically higher than the low equivalent width systems. For example, at median $D \sim 23$ kpc (or $D \sim 0$ kpc) of the USMgII sample, the host galaxies of USMgII systems are a factor 4 (or ~ 10) times higher than absorbers seen in the MAGIICAT sample.

In the MAGIICAT sample, when we consider all cases with W_{2796} measurements and not upper limits, we find that the correlation is stronger between W_{2796} and $D + 0.16(\log(M_*/M_{\odot}) - 10.51)$ (i.e., $r_s = -0.47$ with a p -value of $\sim 10^{-4}$) compared to the correlation between W_{2796} and D (i.e., $r_s = -0.37$ with a p -value of $\sim 10^{-3}$). We repeated the same exercise for USMgII absorbers alone. We find for $W_{2796} - D$ relation the correlation coefficient is $r_s = -0.113$ with p -value = 0.59. After minimizing the mass dependent scatter, (i.e. W_{2796} vs $D + 0.017(\log(M_*/M_{\odot}) - 10.73)$) correlation coefficient is $r_s = -0.112$ with p -value = 0.590.

We quantify this further using the relationship between W_{2796} , D and M_* found by [Huang et al. \(2021\)](#). For the median stellar mass (i.e. $\log(M_*/M_{\odot}) = 10.73$) and impact parameter ($D \sim 24$ kpc), their best-fitted relationship predicts

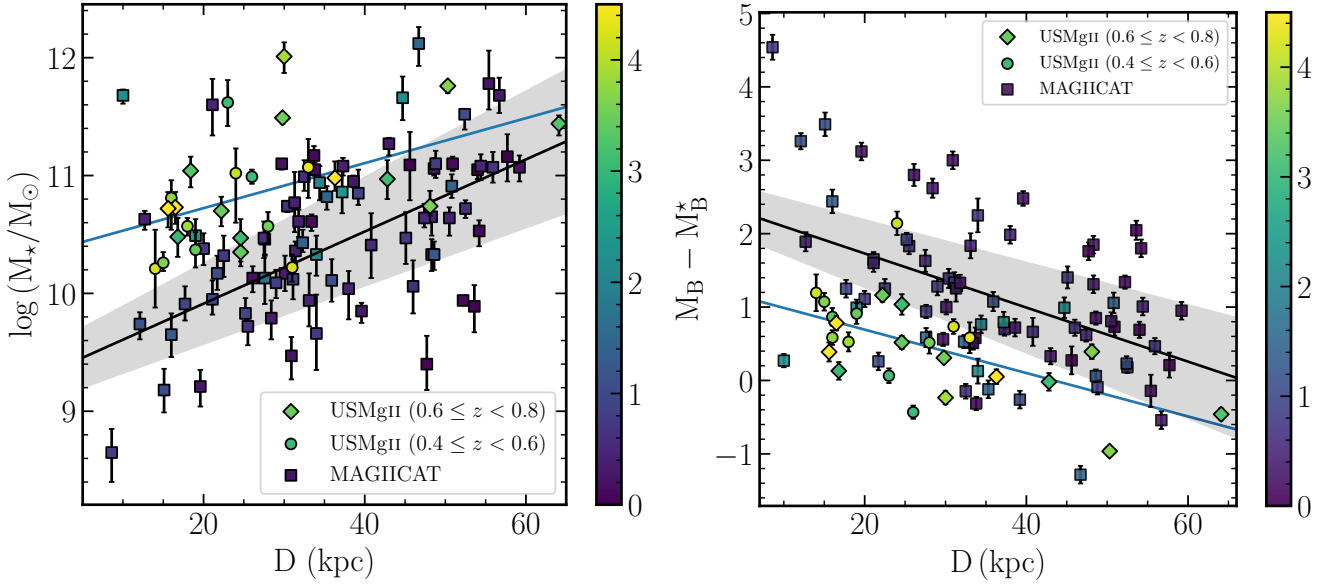


Figure 9. Left panel: Stellar masses of the Mg II host galaxies against their impact parameters, color-coded as W_{2796} . Right Panel: Rest frame absolute B-band magnitudes of the Mg II host galaxies relative to the characteristic B-band magnitude at the same redshift against their impact parameters. For both panels, the diamond, circle, and square markers correspond to the high redshift USMgII host galaxies, low redshift USMgII host galaxies, and the MAGIICAT host galaxies. The solid black lines correspond to the linear regression fit to the MAGIICAT host galaxies, and the grey regions correspond to the 1σ uncertainty to the fit. The solid blue line corresponds to the linear fit, but only for the USMgII host galaxies from our survey.

$W_{2796} \sim 1.15\text{\AA}$. On the contrary, to have $W_{2796} > 3\text{\AA}$ D should be less than 9.5 kpc for the host galaxy with M_* close to the median value of the USMgII host galaxies. While USMgII absorbers are massive for a given impact parameter (as found for the general population of Mg II absorbers), they do not follow the best-fit relationship between W_{2796} , D and M_* obtained for the general Mg II population. This could be related to any prevailing physical conditions specific to USMgII absorbers or some of the high impact parameter USMgII absorbers originating from more than one galaxy.

4.3.4 Dependence on rest frame B-band absolute magnitude

Next, we consider the rest frame absolute B band magnitudes of the USMgII and the host galaxies in the MAGIICAT sample. The rest-frame absolute B band magnitudes (M_B) are obtained from the synthetic SED fitted spectra of the galaxies using the method described in Guha et al. (2022). The rest-frame B-band magnitude for the USMgII host galaxies at $z \sim 0.7$ ranges from $-22.46 \leq M_B \leq -20.27$ with a median value of -21.23 . Upon combining with our $z \sim 0.5$ USMgII host galaxies (Guha et al. 2022), the rest frame B-band magnitude ranges from $-22.46 \leq M_B \leq -19.05$ with a median value of -20.85 . For the MAGIICAT galaxies, M_B ranges $-22.56 \leq M_B \leq -16.53$ with a median value of -20.08 . Column (7) of Table 3 provides the M_B of the USMgII host galaxies identified in this work. Note, as in the case of M_* , M_B measurements are possible only for 26 out of 36 host galaxies as there is the contamination of quasar light in the remaining cases.

In the right panel of Figure 9, we show the scatter plot of M_B relative to the B-band characteristic magnitude (M_B^* , Faber et al. 2007) at the galaxy redshift versus D color-

coded according to the W_{2796} . For the MAGIICAT host galaxies, just like for the stellar mass, we also find a correlation between host galaxy B band absolute magnitude and D , which can be characterized by a linear fit of the form $M_B - M_B^* = (-0.037 \pm 0.008)D$ (kpc) + (2.445 ± 0.302) . The solid black straight line corresponds to this fit, and the gray region associated 1σ uncertainty to the fit. It is evident from the figure that compared to the MAGIICAT host galaxies, for a given D , the USMgII host galaxies tend to be brighter. This aligns with the findings of Chen et al. (2010); Huang et al. (2021), who reported that brighter galaxies produce stronger absorption for a given impact parameter. Like the MAGIICAT host galaxies, we find that $M_B - M_B^*$ of USMgII host galaxies are also anti-correlated with D . A Spearman rank correlation analysis provides $r_s = -0.58$ with p value 0.002. A linear fit to the data for the USMgII galaxies alone gives $M_B - M_B^* = (-0.028 \pm 0.009)D$ (kpc) + (1.234 ± 0.252) . The solid blue line in the left panel of Figure 9 corresponds to this fit. At the median impact parameter for the USMgII host galaxies (i.e., $D=23$ kpc), the host galaxies of the USMgII absorbers are ~ 1 mag brighter than that of the host galaxies in the MAGIICAT sample.

Just like the stellar mass, for the MAGIICAT sample, we find that the anti-correlation is stronger for the quantity D (kpc) $- 0.153(M_B + 20.08)$ and W_{2796} compared to simple $W_{2796} - D$ anti-correlation. The correlation coefficient increases from $r_s = -0.37$ (p -value $\sim 10^{-3}$) to $r_s = -0.49$ (p -value $\sim 10^{-5}$). However, such a linear combination does not significantly alter the correlation coefficients for the USMgII host galaxies. If we use the relationship between W_{2796} , D and M_B found by Huang et al. (2021) the expected W_{2796} is 1.17\AA when we use the median D and M_B . Thus, even though the host galaxies of USMgII are bright at a given D compare

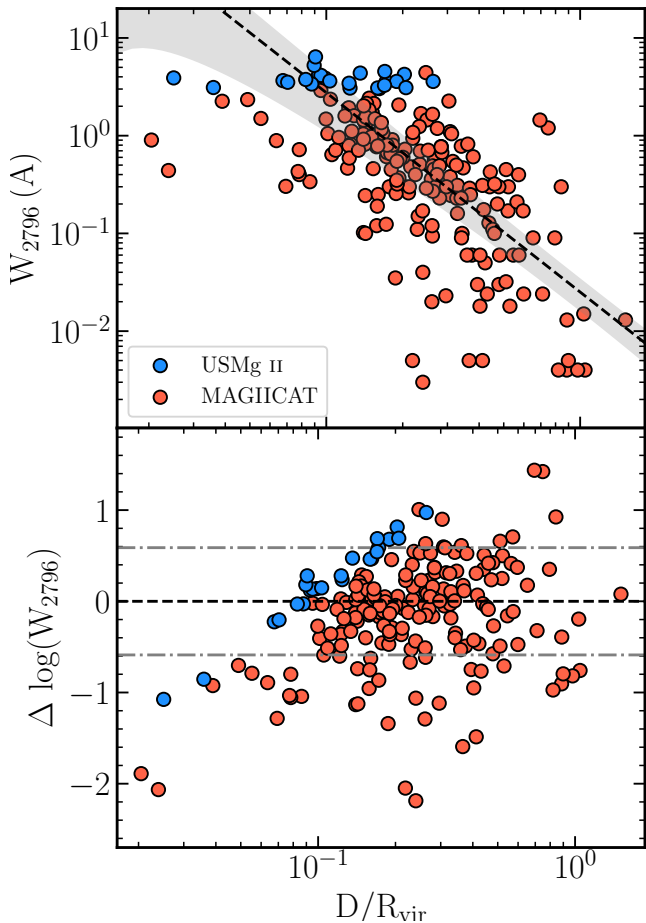


Figure 10. Top panel: Scatter plot of W_{2796} against the normalized impact parameter. Blue points correspond to the USMgII absorbers from our survey and the red points correspond to the MAGIICAT survey. The black dashed line shows the power law fit from Churchill et al. (2013b) with the shaded region corresponding to the 1σ uncertainty. Bottom panel: The difference between the observed $\log(W_{2796})$ and the best-fit model for that normalized impact parameter.

to the host galaxies of normal MgII absorbers they do not follow the relationship between W_{2796} , D and M_B obtained for the general MgII host galaxies.

4.3.5 W_{2796} versus normalized impact parameter

Churchill et al. (2013b) have suggested the scatter in the $W_{2796} - D$ plane is substantially reduced if one uses the normalized impact parameter (i.e. D scaled by the virial radius, R_{vir}) instead of D . In Figure 10, we plot the W_{2796} versus the normalized impact parameter for both the MAGIICAT host galaxies (squares) and the USMgII host galaxies (circle) from our sample. The halo masses for the MAGIICAT host galaxies are obtained from abundance matching techniques (Nielsen et al. 2013b). In contrast, the halo masses for the USMgII galaxies are measured using the stellar mass to halo relations (see Section 4.3.3 and 5.2 for details). Churchill et al. (2013b) found a strong anti-correlation between two quantities best characterized by a power law with a power-law index of ~ -2 (shown in the Figure with an orange dashed line),

albeit a large scatter. When we considered only the USMgII host galaxies, we found no significant anti-correlation (i.e., $r_s = -0.17$ and p-value = 0.59). As the W_{2796} range probed by the USMgII sample is narrow, we expect the scatter in the normalized impact parameter to be lower than that of D if the scaling works as in the case of MAGIICAT host galaxies. In the bottom panel of Figure 10, we show the residual of $\log W_{2796}$ as a function of the normalized impact parameter. The deviation of USMgII point from the best fit is consistent with the scatter seen for the general population of MgII absorbers.

4.3.6 Comparison of USMgII and DLAs:

A large fraction of these USMgII absorbers is expected to be DLAs and sub-DLAs (Rao et al. 2006; Nestor et al. 2007). It is also well known that for a given z , a strong correlation exists between $N(\text{H I})$ and W_{2796} . Using the latest relationship between the two quantities found by Lan & Fukugita (2017) for the USMgII systems, we find $\log N(\text{H I}) \geq 20.20$ at $z \sim 0.7$. Therefore, it is most likely that the USMgII absorbers in our sample are either sub-DLAs or DLAs. It is also well known that DLAs and sub-DLAs show a significant anti-correlation between $N(\text{H I})$ and D (see for example, Rao et al. 2011; Rahmani et al. 2016; Kulkarni et al. 2022).

Information on the impact parameter for these low- z DLA and the sub-DLA host galaxies are obtained from Rahmani et al. (2016), who compiled all the available DLAs and sub-DLAs at low- z from the literature. We obtained W_{2796} for each DLA and sub-DLA from the original references. The W_{2796} associated with the DLAs and the sub-DLAs varies from 0.2\AA to 3.11\AA with a median value of 1.67\AA . In the bottom panel of Figure 5, we plot the $W_{2796} - D$ relationship for DLAs and sub-DLAs at $0.4 \lesssim z \lesssim 1.0$. It is evident from Figure 5 that DLAs and USMgII systems probe similar impact parameter ranges. The KS-test suggests no statistically significant difference between the two impact parameter distributions with a p-value of 0.32. It is clear from Figure 5 that there is no correlation between W_{2796} and D even in the case of low- z DLAs and sub-DLAs. The rank correlation test provides the correlation coefficient of $r_s = -0.17$ and p-value = 0.38. This is consistent with our finding that the anti-correlation weakens when we consider strong Mg II absorbers. Interestingly, for the same DLA sample, the anti-correlation between $N(\text{H I})$ and D is also not statistically significant (with $r_s = -0.31$ and p-value of 0.11 for the Spearman rank correlation test).

At high- z , some of the DLAs selected based on C I absorption and extremely strong DLAs tend to have $W_{2796} > 3\text{\AA}$ (see figure 3 of Ranjan et al. 2022; Zou et al. 2018). Thus lack of USMgII systems among the low- z DLAs mainly identified through MgII based selection (where USMgII systems are a very rare population) is not very surprising. However, the lack of correlation between W_{2796} and D is consistent with our finding in Figure 6. *Discussions presented here clearly demonstrate how system selection influences the derived $w_{2796} - D$ relationship.*

5 DISCUSSION

5.1 Isolated galaxy vs. a group of galaxies

There are indications that some of the strong Mg II absorption systems are associated with multiple host galaxies in literature (e.g., Whiting et al. 2006; Gauthier 2013). Gauthier (2013) have identified a $z \sim 0.5$ galaxy group dominated by passive galaxies associated with a USMgII absorption system and argued that such strong absorption are driven by cool intragroup gas rather than star-formation-driven outflows. Nielsen et al. (2022) have identified a compact galaxy group associated with a DLA, which is also a USMgII system at $z \sim 2.4$, using KCWI and argued the gas in absorption is related to star-formation driven outflows, accretion from the IGM, and the tidal streams due to the galaxy-galaxy interactions. Some of the deviations shown by USMgII absorbers with respect to the relationships found for the general population of Mg II absorbers is not explained if a good fraction of USMgII absorbers is not originating from the CGM of individual galaxies.

Ideally, one requires IFU spectroscopic observations to identify the galaxies contributing to the USMgII absorbers. In recent IFU studies, the only USMgII system present in the MAGG survey (Dutta et al. 2020) and 3 in the sample of Schroetter et al. (2019) are found to be associated with isolated galaxies (no other host galaxy found within 100 kpc and velocity separations within 500 km s^{-1}). In Guha et al. (2022), 33 percent of USMgII absorbers (i.e., 7 out of 21) have only one host galaxy (with $m_r < 23.6$ mag) within an impact parameter of 100 kpc. In Table A2 of the Appendix, we list all the galaxies within a projected distance of 100 kpc at the redshift of the USMgII absorption with $m_r < 23.6$ (typical completeness of the DESI-LIS r-band images) studied in this work. As mentioned before, this sets the completeness of our survey up to $\sim 0.3L_*$ galaxies. Using photometric redshifts, we have found that up to a maximum impact parameter of 100 kpc, for four systems (i.e., along the line of sight to J0055-0100, J1336+0922, J1419+0346, and J2356-0406), there are no galaxies other than the confirmed USMgII host seen in the DESI-LIS images. This gives about $22^{+23}_{-13}\%$ (95% confidence Wilson score) of the USMgII absorption systems originating from isolated galaxies. Therefore, in the combined sample, we have at least 29% of the USMgII systems associated with isolated host galaxies.

On the other hand, in the present sample, 5 out of 18 ($28^{+23}_{-16}\%$) of the USMgII absorbers are confirmed to be associated with multiple galaxies. In the combined sample, this fraction of USMgII absorbers confirmed to be associated with more than one host galaxy is $\geq 21\%$. Among the rest of the six USMgII systems in the present sample, other than the confirmed USMgII host galaxies, there is at least one galaxy with consistent photo- z within 100 kpc with $m_r < 24$. However, we do not have the spectroscopic redshift of these galaxies, so they may or may not be related to the USMgII absorption.

Next, we ask whether there is any difference between the Mg II absorbers properties identified with a single galaxy or multiple galaxies in our sample. Table 5 gives the median values of different measured quantities of the two sub-samples and KS-statistics results (D and p-value). Median values of observed equivalent widths and equivalent width ratios are consistent within 20% uncertainty. This is also reflected by the large p -values found for the KS test. We also find the

Properties	D value	p value	Median (Isolated)	Median (Group)
W_{2796}	0.31	0.62	3.44	3.71
W_{2600}	0.30	0.72	2.22	2.60
W_{2796}/W_{2803}	0.47	0.17	1.07	1.11
W_{2852}/W_{2796}	0.41	0.33	0.30	0.23
D	0.38	0.38	15	27.2
$\log(M_*/M_\odot)$	0.20	1.0	10.47	10.48

Table 5. Comparison of properties of USMgII absorbers associated with single and multiple host galaxies.

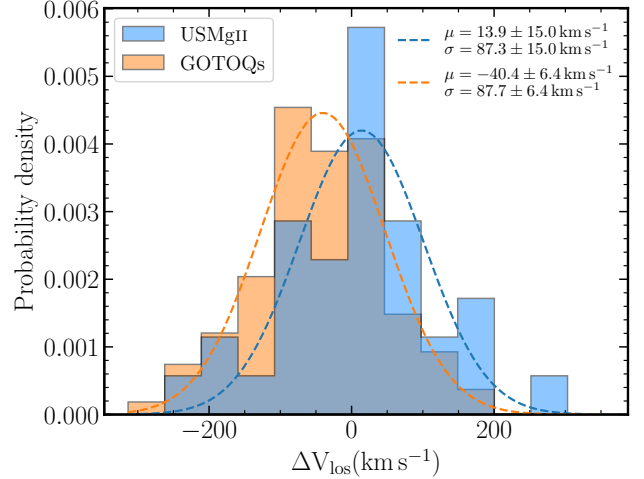


Figure 11. Distribution of the rest frame line of sight velocity offset of the Mg II absorbing gas with respect to the Mg II host galaxies. The blue histogram corresponds to the USMgII host galaxies, whereas the orange histogram corresponds to the GOTOQs. The blue and orange dashed lines correspond to the Gaussian fits to the blue and orange histograms, respectively.

median value of the inferred stellar mass (M_*) of the two samples are almost same. The most significant difference we notice (i.e., by 80%) is for the median value of the impact parameter. The median impact parameter is higher for the nearest galaxy of the USMgII absorber for which more than one host galaxy is identified. Interestingly the difference is not statistically significant due to the small number of systems involved.

5.2 Line of sight velocity of the absorbing gas

Next, we discuss the rest-frame line of sight velocity offset of the absorbing gas with respect to the host galaxies and the fate of the absorbing gas: whether it can escape the host galaxy or is bound to it. In Figure 11, we show the rest-frame line of sight velocity offset of the Mg II absorbing gas with respect to the Mg II host galaxies. The rest-frame velocity offsets are calculated using $\Delta V_{los} = c(z_{abs} - z_{em})/(1 + z_{em})$ where z_{abs} and z_{em} are absorption and emission redshifts obtained from the Mg II absorption towards the quasar line of sights and [O II] nebular emissions of the Mg II host galaxies respectively. c denotes the speed of light. The typical error in this offset measurement is 100 km s^{-1} . The blue histogram corresponds to the USMgII host galaxies, whereas the orange

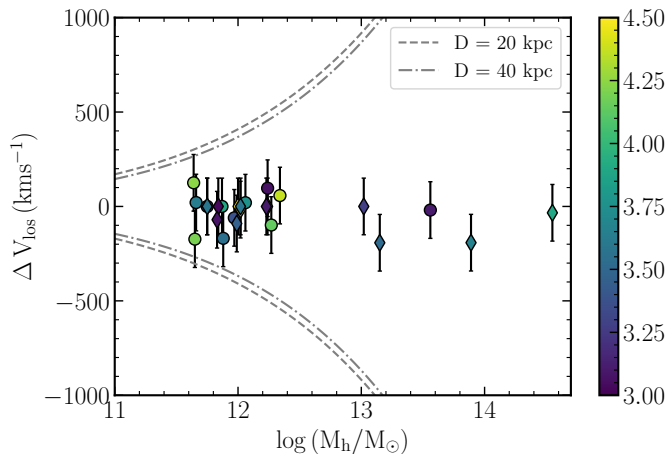


Figure 12. Line of sight velocity offset of the USMgII absorbing gas with respect to the USMgII host galaxies is plotted against the halo masses of the USMgII host galaxies and color-coded according to the W_{2796} respectively correspond to the low and high redshift USMgII absorbers from our sample. Circular and diamond points. The dashed and dot-dashed lines show the escape velocity for a given halo mass at the impact parameters of 20 kpc and 40 kpc, respectively.

histogram corresponds to the GOTOQs. The blue and orange dashed lines correspond to the Gaussian fit of the blue and orange histograms. The line of sight velocity offset for the USMgII absorbers is centered around $\mu \sim 14 \text{ km s}^{-1}$ with a standard deviation of about $\sigma \sim 87 \text{ km s}^{-1}$, whereas for the GOTOQs the center is at $\mu \sim -40 \text{ km s}^{-1}$ with a standard deviation of $\sigma \sim 88 \text{ km s}^{-1}$. The most important thing to notice is that the width of the ΔV_{los} distribution is very similar for the USMgII host galaxies and the GOTOQs. Considering the isolated host galaxies in our sample (discussed above), we find $\mu = 48 \text{ km s}^{-1}$ and $\sigma = 78 \text{ km s}^{-1}$. The same is for the nearest galaxy where the absorber can be associated with more than one galaxy, and we find $\mu = 17 \text{ km s}^{-1}$ and $\sigma = 147 \text{ km s}^{-1}$. The σ being large in the case of absorbers associated with multiple galaxies found here is consistent with the results of (Huang et al. 2021).

Next, we investigate whether or not the absorbing gas is gravitationally bound to the USMgII host galaxies. In Figure 12, we plot the line of sight velocity offset of the USMgII absorbing gas with respect to the USMgII host galaxies against the halo masses of the USMgII host galaxies color-coded according to the W_{2796} . The dashed and the dot-dashed lines show the escape velocity for a given halo mass at the impact parameters of 20 kpc and 40 kpc calculated using an NFW profile (Navarro et al. 1997), respectively. The halo masses are obtained from the stellar mass to halo mass relations at the host galaxy redshifts (Girelli et al. 2020). Note that this relation has a typical uncertainty of 0.2 dex. As seen from Figure 12, the line of sight velocity offset of absorbing gas is insufficient to escape the halo’s gravitational potential. Even if we correct for the three-dimensional velocity components by multiplying ΔV_{los} with a factor of $\sqrt{3}$, all the points are still consistent within 1σ with the absorbing gas to be bound to the host galaxies.

Given the large velocity spread in absorption, it is difficult to imagine that all the gas responsible for the USMgII absorp-

tion will be confined to the host galaxy. For a simple saturated absorption, we expect the USMgII absorption to spread over more than 300 km s^{-1} . However, from Figure 10 of Ranjan et al. (2022), we can see that the velocity spread can be anywhere between 300 to 700 km s^{-1} when $W_{2796} > 3\text{\AA}$. Therefore, high-resolution spectroscopic data are required to directly quantify the fraction of absorbing gas that can be bound to the host galaxy.

5.3 The nature of USMgII host galaxies

Our results indicate that for a given impact parameter USMgII galaxies tend to be more massive and brighter in the B-band compared to the host galaxies of absorbers with low W_{2796} . It is also known that W_{2796} is primarily driven by the total number of such clumps along the line of sight (Pettitjean & Bergeron 1990; Churchill et al. 2020) and velocity dispersion between them rather than the MgII column density. The requirement of large velocity widths for the USMgII can come from (i) large-scale bi-conical outflow; (ii) gaseous in the CGM under the influence of the large gravitational potential of a massive galaxy; or (iii) as discussed above, large velocity widths can originate from gas in the interacting system of galaxies.

Recent high-resolution TNG50 cosmological simulations by DeFelippis et al. (2021) also found that more massive halos produce stronger and broader MgII absorption. However, the USMgII absorbers are extremely rare in these simulations. High mass halos producing stronger MgII absorption is also suggested by various authors in the literature (e.g., Lan et al. 2014; Dutta et al. 2020; Anand et al. 2021) while studying relatively low W_{2796} systems compared to USMgII systems. However, we find that the USMgII systems do not follow the best fit relationship between W_{2796} , D and M_* and/or M_B (see for example, Huang et al. 2021) followed by low W_{2796} absorbers. We require high spectral resolution data to address the origin of this difference. Also, knowing what fraction of the USMgII absorbers originate from more than one host galaxy (using IFU spectroscopy) will help understand this issue.

Our results also indicate that the star formation rate in the USMgII host galaxies is slightly lower than that of the main sequence galaxies at the same redshift having the same stellar mass. Even when one accounts for the possible bias in the SFR estimations it is clear that USMgII host galaxies will, at best, follow the main sequence. Similar trend is found for the massive MgII host galaxies ($M_* \geq 10^{10} M_\odot$) in the MEGAFLOW survey (Schroetter et al. 2019). Rhodin et al. (2018) also found that the massive galaxies producing DLAs and sub-DLAs at $z \sim 0.7$ also have significantly smaller ongoing star formation rates compared to main-sequence galaxies of the same mass. Anand et al. (2021) found that the covering fractions for strong MgII absorption ($W_{2796} \geq 2 \text{\AA}$) within $D \sim 30 \text{ kpc}$ is similar for both the star-forming and the passive galaxies. This could be related to the fact that these galaxies have been through a phase of rapid star formation and consequently became massive. The star-formation-driven outflows enrich the circumgalactic medium while the star-formation-driven feedback starts quenching the galaxies, and hence the ongoing SFR drops below the main sequence. Another contributing factor to the suppression of the star formation rates could be galaxy-galaxy interactions. If a sig-

nificant fraction of the USMgII host galaxies live in a group environment, the motion of these galaxies through the intra-group medium may cause the gas in the galactic disks to be stripped away, shock heated, and turbulent which henceforth further reduced star formation activity.

6 SUMMARY & CONCLUSIONS

In this work, we extend our previous study (Guha et al. 2022) of USMgII absorbers to a slightly higher redshift range (i.e., $0.6 \leq z \leq 0.8$). From an input sample of 151 USMgII systems observed in the SDSS-DR12 (Zhu & Ménard 2013) in the above-mentioned redshift range, we identified 27 secured USMgII systems. We carried out long-slit observations with SALT to identify the host galaxies. This, combined with the sample presented in Guha et al. (2022), constitutes the most extensive sample of USMgII systems studied to date. Our main findings are summarized below.

1. Among the 27 USMgII systems in the present sample, SALT observations could be completed for 25 systems. Based on the [O II] emission or the Ca II absorption present in the spectra, we have successfully identified the host galaxies for the 18 USMgII systems. For 5 of the USMgII systems, we have identified more than one host galaxy associated with the USMgII absorption. The impact parameters of the spectroscopically confirmed USMgII host galaxies range from 6.24 kpc to 120.7 kpc (see Table 3).

2. Inclusion of USMgII data points to the measurements available in the literature increases the scatter in the well-known anti-correlation between W_{2796} and D (see Figure 4). When we consider only the USMgII data points, we do not find any significant correlation between W_{2796} and D (see Figure 5). We find that the best-fit value of $W_{2796}(D = 0)$ is higher than the measurement previously quoted in the literature. We also find that the significance of anti-correlation between W_{2796} and D depends on how the sample is defined. If one defines a sample with a higher W_{2796} threshold there is no trend evident between W_{2796} and D (see Figure 6). Similarly we notice that low- z DLAs do not show any anti-correlation between W_{2796} and D .

3. We find for a given impact parameter, the USMgII host galaxies are brighter and more massive compared to the low equivalent width Mg II absorbers. Such a mass dependence is also seen among the non-USMgII absorbers. However, we find the USMgII absorbers not to follow the relationship between W_{2796} , D and M_* (or M_B) found for the general population of Mg II absorbers (see Figure 9).

4. Although USMgII absorbers do not follow the canonical $W_{2796} - D$ anti-correlations, they seem to follow the $W_{2796} - D/R_{vir}$ anti-correlation. The scatter seen for the USMgII around the global best-fit solution is similar to the scatter seen for the low equivalent width Mg II absorbers. This once again indicates more gaseous content in massive galaxies (see Figure 10).

5. We find that parameters α and β that fit the $W_{2796} - D$ anti-correlation does not evolve significantly with redshift over the redshift range $0 < z \lesssim 1.5$ (see Figure 4). However, even small differences in α can lead to large differences in W_{2796} at high D . For $D > 20$ kpc, the fits are consistent with the W_{2796} at higher redshift being higher for a given

impact parameter. Using a simple model, we argue that major evolution in dn/dz of the Mg II absorbers can come from the evolution of the galaxy luminosity function. The differential evolution seen between high and low equivalent width systems will require a covering factor as a function of D to evolve with time, as found by Lan et al. (2014).

6. Majority of the USMgII host galaxies are detected based on their [O II] emissions, which indicates that they are all star-forming galaxies. However, in the SFR- M_* plane, USMgII host galaxies fall slightly below the main sequence galaxies. We, therefore, infer that the USMgII host galaxies are likely to be post-starburst galaxies transitioning slowly from the main sequence to the quenched galaxies (see Figure 3).

7. Based on the line of sight velocity differences between the absorbing gas and the host galaxies, we find that the overall USMgII absorbing gas is bound to the host galaxies. However, we expect the velocity width of the Mg II absorption to be very large. Most likely, some of the absorbing gas components may have excess velocities outside the escape velocity predicted based on the $M_* - M_h$ relationship. The spectral resolution of our spectra does not allow us to quantify the fraction of gas in each USMgII absorber that is bound to the galaxy. For this, we need higher-resolution spectra (see Figure 12).

8. In our combined USMgII sample, at least 28% of the absorbers are associated with a single isolated galaxy. No other galaxy with correct spectroscopic or photometric redshift having $m_r < 23.6$ is found. Similarly, in the $\sim 21\%$ case, we have identified more than two host galaxies within an impact parameter of 100 kpc. In the remaining 50% cases, our spectroscopic observations are not available for potential candidate host galaxies at $50 \leq D[\text{kpc}] \leq 100$. Completing spectroscopic observations of some of these galaxies will be important to quantify the origin of large velocity fields in USMgII absorbers.

DATA AVAILABILITY

Data used in this work are obtained using SALT. Raw data will become available for public use 1.5 years after the observing date at <https://ssda.sao.ac.za/>.

ACKNOWLEDGEMENT

This project makes use of the following softwares : NumPy (Harris et al. 2020), SciPy (Virtanen et al. 2020), Matplotlib (Hunter 2007), AstroPy (Astropy Collaboration et al. 2013, 2018), and Ultranest (Buchner 2021).

All the new observations reported in this paper were obtained with the Southern African Large Telescope (SALT).

PPJ thanks Camille Noûs (Laboratoire Cogitamus) for inappreciable and often unnoticed discussions, advice, and support. PPJ is partly supported by the Agence Nationale de la Recherche under contract HZ-3D-MAP, ANR-22-CE31-0009.

This paper makes use of SDSS observational data. Funding for the Sloan Digital Sky Survey IV has been provided by the Alfred P. Sloan Foundation, the U.S. Department of Energy Office of Science, and the Participating Institutions. SDSS-IV acknowledges support and resources from

the Center for High-Performance Computing at the University of Utah. The SDSS website is www.sdss.org. SDSS-IV is managed by the Astrophysical Research Consortium for the Participating Institutions of the SDSS Collaboration, including the Brazilian Participation Group, the Carnegie Institution for Science, Carnegie Mellon University, Center for Astrophysics | Harvard & Smithsonian, the Chilean Participation Group, the French Participation Group, Instituto de Astrofísica de Canarias, The Johns Hopkins University, Kavli Institute for the Physics and Mathematics of the Universe (IPMU) / University of Tokyo, the Korean Participation Group, Lawrence Berkeley National Laboratory, Leibniz Institut für Astrophysik Potsdam (AIP), Max-Planck-Institut für Astronomie (MPIA Heidelberg), Max-Planck-Institut für Astrophysik (MPA Garching), Max-Planck-Institut für Extraterrestrische Physik (MPE), National Astronomical Observatories of China, New Mexico State University, New York University, University of Notre Dame, Observatório Nacional / MCTI, The Ohio State University, Pennsylvania State University, Shanghai Astronomical Observatory, United Kingdom Participation Group, Universidad Nacional Autónoma de México, University of Arizona, University of Colorado Boulder, University of Oxford, University of Portsmouth, University of Utah, University of Virginia, University of Washington, University of Wisconsin, Vanderbilt University, and Yale University.

The DESI Legacy Imaging Surveys consist of three individual and complementary projects: the Dark Energy Camera Legacy Survey (DECaLS), the Beijing-Arizona Sky Survey (BASS), and the Mayall z-band Legacy Survey (MzLS). DECaLS, BASS, and MzLS together include data obtained, respectively, at the Blanco telescope, Cerro Tololo Inter-American Observatory, NSF’s NOIRLab; the Bok telescope, Steward Observatory, University of Arizona; and the Mayall telescope, Kitt Peak National Observatory, NOIRLab. NOIRLab is operated by the Association of Universities for Research in Astronomy (AURA) under a cooperative agreement with the National Science Foundation. Pipeline processing and analyses of the data were supported by NOIRLab and the Lawrence Berkeley National Laboratory (LBNL). Legacy Surveys also uses data products from the Near-Earth Object Wide-field Infrared Survey Explorer (NEOWISE), a project of the Jet Propulsion Laboratory/California Institute of Technology, funded by the National Aeronautics and Space Administration. Legacy Surveys was supported by: the Director, Office of Science, Office of High Energy Physics of the U.S. Department of Energy; the National Energy Research Scientific Computing Center, a DOE Office of Science User Facility; the U.S. National Science Foundation, Division of Astronomical Sciences; the National Astronomical Observatories of China, the Chinese Academy of Sciences and the Chinese National Natural Science Foundation. LBNL is managed by the Regents of the University of California under contract to the U.S. Department of Energy. The complete acknowledgments can be found at <https://www.legacysurvey.org/acknowledgment/>. The Photometric Redshifts for the Legacy Surveys (PRLS) catalog used in this paper was produced thanks to funding from the U.S. Department of Energy Office of Science, Office of High Energy Physics via grant DE-SC0007914.

REFERENCES

- Alam S., et al., 2015, *ApJS*, **219**, 12
- Anand A., Nelson D., Kauffmann G., 2021, *MNRAS*, **504**, 65
- Anglés-Alcázar D., Faucher-Giguère C.-A., Kereš D., Hopkins P. F., Quataert E., Murray N., 2017, *Monthly Notices of the Royal Astronomical Society*, **470**, 4698
- Astropy Collaboration et al., 2013, *A&A*, **558**, A33
- Astropy Collaboration et al., 2018, *AJ*, **156**, 123
- Bergeron J., Boissé P., 1991, *A&A*, **243**, 344
- Bouché N., Murphy M. T., Péroux C., Davies R., Eisenhauer F., Förster Schreiber N. M., Tacconi L., 2007, *ApJ*, **669**, L5
- Bouché N., et al., 2012, *MNRAS*, **419**, 2
- Bruzual G., Charlot S., 2003, *Monthly Notices of the Royal Astronomical Society*, **344**, 1000
- Buchner J., 2021, *The Journal of Open Source Software*, **6**, 3001
- Buckley D. A. H., Charles P. A., Nordsieck K. H., O’Donoghue D., 2005, *Proceedings of the International Astronomical Union*, **1**, 1–12
- Burchett J. N., Rubin K. H. R., Prochaska J. X., Coil A. L., Vaught R. R., Hennawi J. F., 2021, *ApJ*, **909**, 151
- Burgh E. B., Nordsieck K. H., Koblunicky H. A., Williams T. B., O’Donoghue D., Smith M. P., Percival J. W., 2003, in Iye M., Moorwood A. F. M., eds, *Society of Photo-Optical Instrumentation Engineers (SPIE) Conference Series Vol. 4841, Instrument Design and Performance for Optical/Infrared Ground-based Telescopes*. pp 1463–1471, doi:10.1117/12.460312
- Calzetti D., 1997, *AJ*, **113**, 162
- Carnall A. C., McLure R. J., Dunlop J. S., Davé R., 2018, *Monthly Notices of the Royal Astronomical Society*, **480**, 4379
- Carnall A. C., Leja J., Johnson B. D., McLure R. J., Dunlop J. S., Conroy C., 2019, *ApJ*, **873**, 44
- Chen H.-W., Helsby J. E., Gauthier J.-R., Shectman S. A., Thompson I. B., Tinker J. L., 2010, *The Astrophysical Journal*, **714**, 1521
- Chevallard J., Charlot S., 2016, *Monthly Notices of the Royal Astronomical Society*, **462**, 1415
- Chisholm J., Prochaska J. X., Schaerer D., Gazagnes S., Henry A., 2020, *MNRAS*, **498**, 2554
- Churchill C. W., Nielsen N. M., Kacprzak G. G., Trujillo-Gomez S., 2013a, *ApJ*, **763**, L42
- Churchill C. W., Trujillo-Gomez S., Nielsen N. M., Kacprzak G. G., 2013b, *The Astrophysical Journal*, **779**, 87
- Churchill C. W., Evans J. L., Stemmock B., Nielsen N. M., Kacprzak G. G., Murphy M. T., 2020, *ApJ*, **904**, 28
- Comparat J., et al., 2016, *MNRAS*, **461**, 1076
- Crawford S. M., et al., 2010, in *Observatory Operations: Strategies, Processes, and Systems III*. p. 773725, doi:10.1117/12.857000
- DeFelippis D., Bouché N. F., Genel S., Bryan G. L., Nelson D., Marinacci F., Hernquist L., 2021, *ApJ*, **923**, 56
- Dey A., et al., 2019, *AJ*, **157**, 168
- Dutta R., et al., 2020, *MNRAS*, **499**, 5022
- Dutta R., et al., 2023, *MNRAS*, **522**, 535
- Faber S. M., et al., 2007, *ApJ*, **665**, 265
- Faucher-Giguère C.-A., Oh S. P., 2023, *arXiv e-prints*, p. arXiv:2301.10253
- Gauthier J.-R., 2013, *Monthly Notices of the Royal Astronomical Society*, **432**, 1444
- Gilbank D. G., Baldry I. K., Balogh M. L., Glazebrook K., Bower R. G., 2010, *MNRAS*, **405**, 2594
- Girelli G., Pozzetti L., Bolzonella M., Giocoli C., Marulli F., Baldi M., 2020, *A&A*, **634**, A135
- Guha L. K., Srianand R., 2023, *MNRAS*, **519**, 3319
- Guha L. K., Srianand R., Dutta R., Joshi R., Noterdaeme P., Petitjean P., 2022, *MNRAS*, **513**, 3836
- Harris C. R., et al., 2020, *Nature*, **585**, 357–362
- Huang Y.-H., Chen H.-W., Shectman S. A., Johnson S. D., Zahedy F. S., Helsby J. E., Gauthier J.-R., Thompson I. B., 2021,

- MNRAS, 502, 4743
- Hunter J. D., 2007, *Computing in Science Engineering*, 9, 90
- Joshi R., Srianand R., Petitjean P., Noterdaeme P., 2017, *Monthly Notices of the Royal Astronomical Society*, 471, 1910
- Joshi R., Srianand R., Petitjean P., Noterdaeme P., 2018, *MNRAS*, 476, 210
- Kacprzak G. G., Churchill C. W., Nielsen N. M., 2012, *ApJ*, 760, L7
- Kacprzak G. G., Cooke J., Churchill C. W., Ryan-Weber E. V., Nielsen N. M., 2013, *The Astrophysical Journal*, 777, L11
- Kennicutt Robert C. J., 1998, *ApJ*, 498, 541
- Kobulnicky H. A., Nordsieck K. H., Burgh E. B., Smith M. P., Percival J. W., Williams T. B., O’Donoghue D., 2003, in Iye M., Moorwood A. F. M., eds, *Society of Photo-Optical Instrumentation Engineers (SPIE) Conference Series Vol. 4841, Instrument Design and Performance for Optical/Infrared Ground-based Telescopes*. pp 1634–1644, doi:10.1117/12.460315
- Kroupa P., Boily C. M., 2002, *MNRAS*, 336, 1188
- Kulkarni V. P., Bowen D. V., Straka L. A., York D. G., Gupta N., Noterdaeme P., Srianand R., 2022, *ApJ*, 929, 150
- Lan T.-W., 2020, *ApJ*, 897, 97
- Lan T.-W., Fukugita M., 2017, *ApJ*, 850, 156
- Lan T.-W., Ménard B., Zhu G., 2014, *ApJ*, 795, 31
- Lehner N., et al., 2013, *ApJ*, 770, 138
- Lundgren B. F., et al., 2012, *ApJ*, 760, 49
- Lundgren B. F., et al., 2021, *ApJ*, 913, 50
- Marigo P., Bressan A., Nanni A., Girardi L., Pumo M. L., 2013, *Monthly Notices of the Royal Astronomical Society*, 434, 488
- Moustakas J., Kennicutt Robert C. J., Tremonti C. A., 2006, *ApJ*, 642, 775
- Ménard B., Wild V., Nestor D., Quider A., Zibetti S., Rao S., Turnshek D., 2011, *Monthly Notices of the Royal Astronomical Society*, 417, 801
- Navarro J. F., Frenk C. S., White S. D. M., 1997, *ApJ*, 490, 493
- Nestor D. B., Turnshek D. A., Rao S. M., Quider A. M., 2007, *The Astrophysical Journal*, 658, 185–202
- Nestor D. B., Johnson B. D., Wild V., Ménard B., Turnshek D. A., Rao S., Pettini M., 2011b, *MNRAS*, 412, 1559
- Nestor D. B., Johnson B. D., Wild V., Ménard B., Turnshek D. A., Rao S., Pettini M., 2011a, *Monthly Notices of the Royal Astronomical Society*, 412, 1559
- Nielsen N. M., Churchill C. W., Kacprzak G. G., 2013a, *The Astrophysical Journal*, 776, 115
- Nielsen N. M., Churchill C. W., Kacprzak G. G., 2013b, *The Astrophysical Journal*, 776, 115
- Nielsen N. M., Kacprzak G. G., Sameer Murphy M. T., Nateghi H., Charlton J. C., Churchill C. W., 2022, *MNRAS*, 514, 6074
- Osterbrock D. E., Ferland G. J., 2006, *Astrophysics of gaseous nebulae and active galactic nuclei*
- Péroux C., Howk J. C., 2020, *ARA&A*, 58, 363
- Petitjean P., Bergeron J., 1990, *A&A*, 231, 309
- Rahmani H., et al., 2016, *MNRAS*, 463, 980
- Ranjan A., et al., 2022, *A&A*, 661, A134
- Rao S. M., Turnshek D. A., Nestor D. B., 2006, *ApJ*, 636, 610
- Rao S. M., Belfort-Mihalyi M., Turnshek D. A., Monier E. M., Nestor D. B., Quider A., 2011, *MNRAS*, 416, 1215
- Rhodin N. H. P., Christensen L., Møller P., Zafar T., Fynbo J. P. U., 2018, *A&A*, 618, A129
- Rubin K. H. R., Prochaska J. X., Koo D. C., Phillips A. C., Weiner B. J., 2010, *The Astrophysical Journal*, 712, 574
- Rubin K. H. R., Prochaska J. X., Koo D. C., Phillips A. C., 2012, *ApJ*, 747, L26
- Rubin K. H. R., Prochaska J. X., Koo D. C., Phillips A. C., Martin C. L., Winstrom L. O., 2014, *The Astrophysical Journal*, 794, 156
- Rubin K. H. R., Diamond-Stanic A. M., Coil A. L., Crighton N. H. M., Moustakas J., 2018, *ApJ*, 853, 95
- Schroetter I., Bouché N., Péroux C., Murphy M. T., Contini T., Finley H., 2015, *ApJ*, 804, 83
- Schroetter I., et al., 2019, *MNRAS*, 490, 4368
- Science Software Branch at STScI 2012, PyRAF: Python alternative for IRAF, Astrophysics Source Code Library, record ascl:1207.011 (ascl:1207.011)
- Speagle J. S., Steinhardt C. L., Capak P. L., Silverman J. D., 2014, *ApJS*, 214, 15
- Steidel C. C., 1995, in Meylan G., ed., *QSO Absorption Lines*. p. 139 (arXiv:astro-ph/9509098)
- Tremonti C. A., Moustakas J., Diamond-Stanic A. a. M., 2007, *The Astrophysical Journal*, 663, L77
- Tumlinson J., Peebles M. S., Werk J. K., 2017, *ARA&A*, 55, 389
- Virtanen P., et al., 2020, *Nature Methods*, 17, 261
- Whiting M. T., Webster R. L., Francis P. J., 2006, *MNRAS*, 368, 341
- Wisotzki L., et al., 2018, *Nature*, 562, 229
- York D. G., et al., 2000, *AJ*, 120, 1579
- Zahedy F. S., Chen H.-W., Johnson S. D., Pierce R. M., Rauch M., Huang Y.-H., Weiner B. J., Gauthier J.-R., 2019, *MNRAS*, 484, 2257
- Zhu G., Ménard B., 2013, *ApJ*, 770, 130
- Zou S., Petitjean P., Noterdaeme P., Ledoux C., Krogager J. K., Fathivavsari H., Srianand R., López S., 2018, *A&A*, 616, A158

APPENDIX A: BAL QUASARS AS FALSE USMgII ABSORPTION SYSTEMS IN THE SDSS ABSORBERS CATALOG

Table A1 provides the details of all the 151 USMgII absorption systems in the redshift range $0.6 \geq z_{abs} \geq 0.8$ that is accessible to the SALT (declination $\delta \leq 10^\circ$) from SDSS-DR12 Fe II / Mg II metal absorber catalog (Zhu & Ménard 2013). For each of the listed absorption systems, we explicitly mention the reasoning for whether the system is included in our sample or not.

Table A1. Details of all the 151 USMgII absorbers from [Zhu & Ménard \(2013\)](#) in the redshift range $0.6 \leq z_{abs} \leq 0.8$ with declination, $\delta \leq 10^\circ$.

No.	Quasar	Plate	Fiber	MJD	z_{qso}	z_{abs}	Comment
1	J001030.81+012203.43	4298	322	55511	2.197	0.6431	Secure USMgII identification.
2	J000931.24+031420.14	4297	182	55806	2.323	0.7752	False identification of USMgII absorption.
3	J001156.33-013701.47	4365	874	55539	2.305	0.7837	BAL quasar
4	J001227.00+092701.75	4536	650	55857	2.453	0.7365	False identification of USMgII absorption.
5	J001232.06+052657.94	4416	320	55828	2.621	0.7952	BAL quasar
6	J001436.53-090622.34	7169	890	56628	2.518	0.7283	BAL quasar
7	J001602.40-001225.10	4218	147	55479	2.080	0.6241	False identification of USMgII absorption.
8	J002022.66+000231.98	4219	734	55480	2.749	0.7699	Secure USMgII system
9	J002410.02+064620.69	4417	796	55829	2.915	0.7606	Blended lines detected as USMgII
		4537	24	55806	2.915	0.7605	
10	J002509.22-071616.78	7150	40	56597	2.130	0.6932	BAL quasar
11	J002529.79+001339.69	4220	618	55447	2.085	0.6691	BAL quasar
12	J002839.24+004103.05	3586	564	55181	2.493	0.6565	Secure USMgII system
		4220	846	55447	2.493	0.6567	
13	J003336.04+013851.06	4302	150	55531	2.658	0.7187	Secure USMgII system
14	J003749.07-065428.97	7152	990	56660	2.331	0.7931	BAL quasar
15	J003904.01+023313.28	4304	681	55506	2.304	0.7917	BAL quasar
16	J004045.20+040646.21	4303	978	55508	2.143	0.6931	BAL quasar
17	J004444.06+001303.59	4222	972	55444	2.280	0.7791	BAL quasar
18	J004618.61-000936.78	4222	10	55444	2.439	0.6256	Blended lines detected as USMgII
19	J005521.73-002817.19	4224	186	55481	2.254	0.7351	BAL quasar
20	J005551.22-002837.17	4224	149	55481	2.428	0.6302	BAL quasar
21	J005554.25-010058.62	4224	170	55481	2.363	0.7150	Secure USMgII system
22	J005958.70+095338.68	4547	726	55893	0.693	0.6844	BAL quasar
23	J010543.52+004003.86	4225	964	55455	1.078	0.6489	Secure USMgII system
		3735	821	55209	1.078	0.6489	
24	J010915.69+055138.52	4423	270	55889	2.324	0.6270	Poor SNR. False identification of USMgII .
25	J011448.97+042018.91	4312	846	55511	2.157	0.7131	BAL quasar
26	J011722.00-012734.86	4353	752	55532	2.179	0.7182	BAL quasar
27	J011903.30-021746.91	4353	859	55532	2.319	0.7909	BAL quasar
28	J012424.98-010327.66	4228	96	55484	2.148	0.7034	BAL quasar
29	J012711.11-055020.95	7047	207	56572	2.137	0.6837	Secure USMgII system
30	J013311.86-054258.13	7048	214	56575	2.139	0.6266	False identification of USMgII
31	J013537.43-003853.06	4230	184	55483	2.276	0.6233	BAL quasar
32	J014115.32-000500.98	3639	773	55205	2.130	0.6105	Secure USMgII system
33	J014118.88-021214.49	4350	659	55556	2.268	0.7721	BAL quasar
34	J014118.88-021214.49	4350	659	55556	2.268	0.7443	BAL quasar
35	J014258.83+094942.43	4545	360	55567	0.981	0.7858	Secure USMgII system
36	J015007.91-003937.09	4232	194	55447	2.730	0.7747	Secure USMgII system
37	J015049.39+060432.42	4403	274	55536	2.676	0.6707	Secure USMgII system
38	J015522.03-034740.11	7052	630	56539	2.433	0.6128	False identification of USMgII
39	J020100.99+020659.50	4271	196	55507	2.149	0.6720	BAL quasar
40	J020733.90-040847.28	7238	869	56660	2.157	0.6195	BAL quasar
41	J020812.49-004928.84	4235	299	55451	2.220	0.7475	BAL quasar
42	J020949.08-054824.53	4398	962	55946	0.738	0.7310	BAL quasar
43	J022419.07+022813.62	4265	740	55505	2.317	0.7225	Poor SNR. False identification of USMgII
44	J022445.16+001028.34	6780	536	56267	2.161	0.7124	BAL quasar
45	J022545.65+005149.96	3647	638	55241	2.525	0.7437	BAL quasar
		3647	610	55476	2.525	0.7436	
		3615	634	55179	2.525	0.7445	
		3647	638	55241	2.525	0.7437	
46	J022812.19+002657.82	3647	722	55476	2.585	0.6402	BAL quasar
47	J023252.80-001351.15	3615	40	56544	2.025	0.6497	BAL quasar
		3615	30	55179	2.025	0.6499	
48	J024004.18+004500.68	4239	958	55458	2.233	0.6887	Blended lines detected as USMgII
		4240	635	55455	2.233	0.6888	

Table A1. Continued.

		3651	556	55247	2.233	0.6888	
		3650	754	55244	2.233	0.6890	
49	J024046.76-062829.65	7055	474	56576	2.579	0.6852	BAL quasar
50	J025607.25+011038.56	4242	784	55476	1.349	0.7256	Secure USMgII system
51	J081214.92+013608.90	4787	404	55863	2.177	0.7250	BAL quasar
52	J081829.68+070655.74	4841	634	55895	2.215	0.6037	False identification of USMgII
53	J081831.10+012608.74	4792	450	55925	2.618	0.7622	Poor SNR. False identification of USMgII .
54	J084502.73+081214.26	5285	952	55946	2.365	0.7034	BAL quasar
55	J085731.54+041951.40	3814	880	55535	2.445	0.7862	Poor SNR. False USMgII identification.
56	J085932.56+064254.29	4868	608	55895	2.034	0.6422	BAL quasar
57	J090805.76+072739.90	5299	215	55927	2.414	0.6122	Secure USMgII system
58	J092550.26+041503.41	4796	376	55924	2.381	0.6833	BAL quasar
59	J092550.26+041503.41	4796	376	55924	2.381	0.6724	BAL quasar
60	J093415.29+090059.49	5314	650	55952	2.268	0.7259	Poor SNR. False USMgII identification.
61	J093955.67-013513.90	3782	554	55244	2.315	0.7364	BAL quasar
62	J094202.95+082643.74	5314	8	55952	2.228	0.7467	Poor SNR. False USMgII identification.
63	J094548.46+023108.29	4736	973	55631	2.631	0.7495	Blended lines detected as USMgII
64	J094852.19+011506.73	4743	348	55645	2.314	0.6891	Poor SNR. False USMgII identification.
65	J095619.49+001800.34	3828	774	55539	2.172	0.7821	Secure USMgII system
66	J095745.89+062811.70	4874	360	55673	2.308	0.7359	BAL quasar
67	J100029.85+095434.30	5327	250	55979	2.320	0.7925	BAL quasar
68	J100154.84-005500.81	3783	750	55246	2.455	0.6444	Blended lines detected as USMgII
69	J100339.82+082236.33	5329	312	55946	2.121	0.6706	BAL quasar
70	J100513.61+004028.31	3829	802	55300	2.568	0.7952	BAL quasar
71	J100716.69+030438.75	4738	646	55650	2.127	0.6109	BAL quasar
72	J102219.71-020735.81	3770	620	55234	2.162	0.6681	BAL quasar
73	J103325.92+012836.35	4734	442	55646	2.180	0.6709	Secure USMgII system
74	J103400.72+032557.35	4772	130	55654	2.370	0.7070	BAL quasar
75	J103433.72-011732.74	3785	918	55241	2.615	0.7831	BAL quasar
		3785	914	55273	2.615	0.7834	
76	J104642.70+045731.96	4773	998	55648	2.542	0.7849	Secure USMgII system
77	J110650.53+061049.86	4855	200	55926	2.251	0.7553	BAL quasar
78	J110728.16+051016.40	4770	600	55928	2.570	0.7131	BAL quasar
79	J111108.20+095513.98	5361	4	55973	2.272	0.7160	BAL quasar
80	J111535.12-011442.50	3838	364	55588	2.291	0.7843	BAL quasar
81	J111627.65+050049.96	4769	526	55931	2.571	0.7208	Secure USMgII system
		4770	990	55928	2.571	0.7207	
82	J114747.38+092108.76	5380	102	55980	2.176	0.7091	BAL quasar
83	J114842.43-023948.03	3790	260	55208	2.197	0.7308	BAL quasar
84	J115026.11+090048.40	5382	714	55982	2.492	0.7569	Secure USMgII system
85	J115911.34+025831.12	4747	364	55652	2.250	0.7104	Poor SNR. False USMgII identification.
86	J120131.70+054123.44	4831	467	55679	2.231	0.7346	BAL quasar
87	J120139.57+071338.24	5389	296	55953	1.205	0.6842	Secure USMgII system
88	J120326.31+052445.77	4831	399	55679	2.118	0.7149	BAL quasar
89	J120403.00+064829.56	5389	166	55953	2.263	0.7625	BAL quasar
90	J121212.09+083216.44	5393	764	55946	2.119	0.6721	BAL quasar
91	J121727.80-011548.57	3777	758	55210	2.624	0.6642	Secure USMgII system
92	J123858.06+064042.34	5407	366	55926	2.250	0.7450	BAL quasar
93	J123917.42-013132.42	3793	524	55214	2.310	0.7910	BAL quasar
94	J124602.10+075425.69	5407	39	55926	2.139	0.7233	BAL quasar
95	J125046.21+024414.37	4756	885	55631	2.332	0.7798	BAL quasar
96	J131216.58-013145.00	4053	742	55591	2.163	0.7089	BAL quasar
97	J132200.79-010755.70	4050	451	55599	2.160	0.7226	Secure USMgII system
98	J132216.24+052446.33	4839	442	55703	2.045	0.6439	BAL quasar
		4761	794	55633	2.045	0.6441	BAL quasar
99	J132251.16+004901.21	4050	586	55599	2.397	0.6627	
100	J133653.73+092221.23	5437	508	55973	2.531	0.7059	Secure USMgII system
101	J134857.12+032234.35	4785	260	55659	2.363	0.7737	BAL quasar
102	J135009.61+092417.23	5442	786	55978	2.415	0.6799	BAL quasar

Table A1. Continued.

103	J140017.69-014902.40	4041	964	55361	2.555	0.7928	Secure USMgII system
104	J141930.09+034643.73	4782	100	55654	2.316	0.7250	Secure USMgII system
105	J142140.27-020239.03	4032	736	55333	2.084	0.6707	BAL quasar
106	J142218.92-025250.56	4032	254	55333	2.380	0.6976	False identification of USMgII absorption.
107	J142452.06+025007.78	4027	828	55629	2.287	0.6095	BAL quasar
108	J142735.32-003936.43	4028	131	55621	2.650	0.7883	BAL quasar
109	J143023.18+084219.53	5462	62	55978	2.396	0.7192	Poor SNR. False identification of USMgII
110	J143158.00+075448.29	5467	456	55973	2.522	0.7453	Poor SNR. False identification of USMgII
111	J143223.09-000116.43	4025	613	55350	2.474	0.6455	Blended lines detected as USMgII
112	J143550.09+084854.09	5467	776	55973	2.777	0.7890	False identification of USMgII
113	J143830.68-014807.43	4026	696	55325	2.220	0.7408	BAL quasar
114	J144936.18-011650.46	4023	758	55328	0.772	0.6621	Secure USMgII system
115	J145108.53-013833.06	4023	814	55328	2.390	0.7408	Secure USMgII system
116	J150341.63+063456.57	4856	318	55712	2.463	0.6494	BAL quasar
117	J151841.30+094936.26	5489	210	55990	0.666	0.6418	BAL quasar
118	J152218.01+051007.01	4803	558	55734	2.454	0.6744	BAL quasar
119	J152316.86+091030.01	5490	862	56003	2.378	0.7573	False identification of USMgII
120	J153635.03+060412.68	4885	62	55735	2.478	0.6126	BAL quasar
121	J154000.99+070854.50	5211	324	56002	2.122	0.6731	BAL quasar
122	J154143.28+021536.37	4054	977	55358	2.267	0.7847	BAL quasar
123	J155625.89+045248.80	4808	509	55705	2.700	0.7174	BAL quasar
124	J160759.22+054038.63	4895	378	55708	2.446	0.7966	BAL quasar
125	J212521.07+001054.41	4193	778	55476	2.150	0.6385	BAL quasar
126	J214015.57+012024.17	5145	617	55835	2.267	0.7750	BAL quasar
127	J215002.02-010938.48	4197	402	55479	2.426	0.6496	Poor SNR. Blended lines detected as USMgII.
128	J215217.10+042603.13	4096	450	55501	2.596	0.6854	False identification of USMgII
129	J215422.57-003253.53	4197	154	55479	2.833	0.7280	False identification of USMgII
130	J221820.92+044944.33	4319	646	55507	2.193	0.6772	False identification of USMgII
131	J222312.24+094106.93	5052	154	55857	2.609	0.6639	False identification of USMgII
132	J222519.53+004523.99	4202	718	55445	2.132	0.6835	BAL quasar
133	J222635.48+093117.81	5053	452	56213	2.364	0.7261	BAL quasar
134	J224028.14-003813.17	4204	232	55470	0.658	0.6520	BAL quasar
135	J224101.17+075224.97	5059	537	56190	2.176	0.7040	BAL quasar
136	J225211.14+061927.72	4412	886	55912	2.224	0.7195	BAL quasar
137	J225251.12+000501.20	4206	738	55471	2.130	0.6322	BAL quasar
138	J225750.19+032623.61	4293	124	55509	2.563	0.6714	False identification of USMgII
139	J230027.63-022610.26	4362	280	55828	2.163	0.6246	BAL quasar
140	J230143.68-003909.52	4208	484	55476	2.276	0.6663	False identification of USMgII
141	J231014.92+070746.11	6168	350	56187	2.388	0.6741	False identification of USMgII
142	J231155.29+090153.81	6163	496	56219	2.222	0.6973	False identification of USMgII
143	J231355.83-022039.10	4360	360	55539	2.275	0.7483	BAL quasar
144	J232107.95-002756.62	4210	196	55444	2.285	0.6494	False identification of USMgII
145	J232117.95+035840.72	4285	734	55881	2.119	0.6089	BAL quasar
146	J232339.29+045126.75	4285	870	55881	2.891	0.7550	Blended lines detected as USMgII
147	J233739.99-002701.16	4213	396	55449	2.510	0.6502	BAL quasar
148	J234603.48-000258.01	4213	11	55449	2.081	0.6666	BAL quasar
149	J234626.48+052737.48	4406	854	55858	2.221	0.7471	BAL quasar
150	J235242.02-103837.72	7166	298	56602	2.919	0.7784	BAL quasar
151	J235639.31-040614.47	7034	506	56564	2.880	0.7709	Secure USMgII system

APPENDIX B: DETECTION OF USMgII HOST GALAXIES BASED ON THE Ca II ABSORPTION**APPENDIX C: MISC**

This paper has been typeset from a \LaTeX file prepared by the author.

As mentioned in Section 4.1, we identify the USMgII host galaxies based on the emission lines present in the spectra of the candidate galaxies except for two cases (J0055–0100 and J0142+0949). In Figure B1, we show the spectra of these two USMgII host galaxies and the Ca II absorption present in them.

Table A2. Details of galaxies around the USMgII absorption systems in our sample with $D < 100$ kpc with $m_r < 24$

No.	Quasar Name	z_{abs}	Galaxy coordinates	m_r	D(kpc)	Photo-z	Comments
1	J0020+0002	0.7699	J002022.50+000235.52	23.19	31.5	0.619 ± 0.233	Consistent
			J002022.65+000230.68	23.39	9.7	1.152 ± 0.180	Spectroscopically confirmed
2	J0028+0041	0.6565	J002839.78+004057.62	23.78	68.0	1.063 ± 0.148	Inconsistent
			J002838.78+004100.76	21.92	50.1	0.410 ± 0.110	Inconsistent
			J002839.05+004104.58	22.73	22.2	0.765 ± 0.128	Spectroscopically confirmed
			J002839.13+004049.56	23.55	94.5	0.812 ± 0.410	Consistent
3	J0033+0138	0.7187	J002839.53+004115.93	23.39	94.7	0.599 ± 0.228	Consistent
			J003336.24+013844.75	20.96	50.3	0.784 ± 0.057	Spectroscopically confirmed
			J003335.83+013838.37	22.83	94.5	0.818 ± 0.057	Inconsistent
			J003335.90+013900.31	23.82	68.6	1.129 ± 0.653	Consistent
4	J0055-0100	0.7150	J003335.90+013847.27	22.01	31.4	0.427 ± 0.077	Inconsistent
			J003336.11+013843.10	23.86	57.9	1.079 ± 0.216	Inconsistent
			J005554.95-010052.02	23.46	89.7	1.020 ± 0.242	Inconsistent
			J005554.28-010102.72	22.24	29.8	0.697 ± 0.032	Spectroscopically confirmed
5	J0105+0040	0.6489	J005554.44-010056.53	23.96	25.7	0.962 ± 0.211	Inconsistent
			J010542.82+004011.05	23.78	87.9	0.981 ± 0.116	Inconsistent
			J010543.05+004016.30	23.52	99.0	0.635 ± 0.205	Consistent
			J010543.09+004005.21	22.27	44.8	0.578 ± 0.219	Consistent
6	J0127-0550	0.6837	J010543.27+004002.93	22.45	25.9	1.033 ± 0.287	Inconsistent
			J010543.48+004013.75	23.04	68.6	0.926 ± 0.091	Inconsistent
			J010543.67+004001.10	21.79	24.6	0.658 ± 0.154	Spectroscopically confirmed
			J010543.97+003957.28	22.45	65.7	0.541 ± 0.251	Spectroscopically confirmed
7	J0142+0949	0.7858	J010544.11+003953.44	22.52	94.7	0.627 ± 0.172	Consistent
			J012711.91-055016.45	22.17	90.1	0.733 ± 0.092	Spectroscopically confirmed
			J012711.20-055019.01	21.52	16.8	0.678 ± 0.073	Spectroscopically confirmed
			J012711.65-055029.19	22.48	81.6	0.647 ± 0.115	Consistent
8	J0150-0039	0.7747	J014258.56+094942.20	22.52	30.0	0.905 ± 0.057	Spectroscopically confirmed
			J014258.58+094949.01	23.51	56.5	0.807 ± 0.103	Consistent
			J014258.60+094936.54	23.85	50.7	0.886 ± 0.128	Consistent
			J014259.09+094947.92	22.66	50.1	0.669 ± 0.470	Consistent
9	J0150+0604	0.6707	J015007.31-003935.11	23.95	68.5	1.024 ± 0.404	Consistent
			J015007.44-003931.92	21.66	65.5	0.694 ± 0.032	Inconsistent
			J015007.92-003935.52	23.71	11.7	0.916 ± 0.201	Consistent
			J015008.43-003931.82	23.41	70.0	1.057 ± 0.676	Consistent
10	J0256+0110	0.7256	J015008.60-003929.18	23.68	96.5	1.134 ± 0.153	Inconsistent
			J015048.84+060443.27	22.67	95.4	0.783 ± 0.073	Inconsistent
			J015048.92+060442.74	22.33	87.4	0.563 ± 0.256	Consistent
			J025608.12+011034.20	23.98	99.3	0.967 ± 0.124	Inconsistent
11	J0908+0727	0.6122	J025606.80+011038.87	22.95	48.8	0.680 ± 0.057	Consistent
			J025607.10+011039.80	22.18	18.4	0.727 ± 0.051	Spectroscopically confirmed
			J025607.52+011027.60	22.43	84.7	0.707 ± 0.032	Consistent
			J025607.91+011036.25	23.83	73.1	1.231 ± 0.602	Consistent
12	J0956+0018	0.7821	J090805.91+072740.58	22.12	16.5	0.568 ± 0.068	Spectroscopically confirmed
			J090806.07+072732.04	23.57	61.6	0.658 ± 0.237	Consistent
			J095619.41+001802.00	22.50	15.6	0.619 ± 0.096	Spectroscopically confirmed
			J095619.67+001806.24	22.98	48.0	0.709 ± 0.170	Consistent
13	J1033+0128	0.6709	J095619.92+001754.41	21.87	65.0	0.310 ± 0.146	Inconsistent
			J103325.50+012839.08	21.63	48.5	1.030 ± 0.294	Inconsistent
			J103325.65+012839.82	23.80	38.0	0.937 ± 0.157	Inconsistent
			J103325.67+012835.11	21.79	27.7	0.635 ± 0.092	Consistent
14	J1046+0457	0.7848	J103325.85+012833.25	23.14	23.3	0.619 ± 0.198	Consistent
			J104642.79+045719.64	22.93	92.6	0.607 ± 0.314	Consistent
			J104642.52+045739.54	21.54	60.0	0.501 ± 0.278	Consistent
			J111627.24+050050.21	23.74	43.6	0.687 ± 0.321	Consistent
15	J1116+0500	0.7208	J111627.78+050050.44	23.84	14.6	0.928 ± 0.160	Inconsistent

Table A2. Continued.

No.	Quasar Name	z_{abs}	Galaxy coordinates	m_r	D(kpc)	Photo-z	Comments
16	J1150+0900	0.7569	J115026.23+090042.52	22.93	45.2	1.124 ± 0.498	Consistent
17	J1201+0713	0.6842	J120139.96+071328.30	20.86	81.4	0.467 ± 0.054	Inconsistent
			J120139.11+071344.91	23.19	67.7	0.813 ± 0.184	Consistent
			J120139.41+071342.84	21.67	36.6	0.653 ± 0.089	Spectroscopically confirmed
			J120139.77+071333.28	21.75	41.3	0.697 ± 0.049	Spectroscopically confirmed
18	J1217-0115	0.6642	J121727.02-011553.88	19.87	90.2	0.308 ± 0.035	Inconsistent
			J121727.21-011556.15	23.65	81.2	1.033 ± 0.431	Consistent
			J121727.78-011558.88	19.42	72.1	0.070 ± 0.069	Inconsistent
			J121727.96-011551.50	22.97	26.1	0.800 ± 0.108	Inconsistent
			J121728.19-011545.93	23.97	44.9	1.110 ± 0.351	Inconsistent
			J121728.60-011550.74	23.33	85.0	0.945 ± 0.120	Inconsistent
19	J1322-0107	0.7226	J132200.59-010753.28	22.92	28.2	0.526 ± 0.144	Inconsistent
			J132200.90-010748.64	22.14	52.3	0.266 ± 0.227	Inconsistent
20	J1336+0922	0.7059	J133653.38+092229.76	23.54	71.6	0.960 ± 0.132	Inconsistent
			J133653.59+092215.03	22.71	46.9	0.828 ± 0.097	Inconsistent
			J133653.80+092217.96	22.69	24.6	0.701 ± 0.128	Spectroscopically confirmed
21	J1400-0149	0.7928	J140016.86-014859.22	23.74	96.3	0.849 ± 0.474	Consistent
			J140017.98-014853.62	23.95	73.2	0.842 ± 0.348	Consistent
22	J1419+0346	0.7250	J141929.42+034645.82	23.63	73.7	1.020 ± 0.160	Inconsistent
			J141929.46+034648.31	23.54	75.7	0.930 ± 0.158	Inconsistent
			J141929.62+034641.15	23.37	54.2	0.894 ± 0.082	Inconsistent
			J141930.39+034639.86	21.82	42.8	0.767 ± 0.073	Spectroscopically confirmed
23	J1449-0116	0.6621	J144935.43-011652.92	23.88	80.7	1.116 ± 0.230	Inconsistent
			J144935.61-011643.87	23.88	75.9	0.981 ± 0.115	Inconsistent
			J144935.69-011702.53	23.45	99.1	0.845 ± 0.202	Consistent
			J144935.92-011637.35	22.08	95.7	0.408 ± 0.098	Inconsistent
			J144936.20-011643.58	21.85	48.1	0.559 ± 0.086	Spectroscopically confirmed
			J144936.52-011652.65	23.64	37.9	0.615 ± 0.227	Consistent
			J144937.02-011646.41	22.79	92.1	0.539 ± 0.258	Consistent
24	J1451-0138	0.7408	J145108.15-013836.17	21.92	47.9	0.480 ± 0.063	Inconsistent
			J145108.24-013840.64	21.59	64.1	0.811 ± 0.058	Spectroscopically confirmed
			J145108.52-013841.80	19.30	63.8	0.191 ± 0.035	Inconsistent
			J145108.62-013831.19	20.76	16.7	0.248 ± 0.164	Inconsistent
			J145109.00-013831.22	22.62	53.2	0.558 ± 0.088	Inconsistent
			J145109.35-013837.29	22.71	95.0	0.574 ± 0.235	Consistent
25	J2356-0406	0.7059	J235639.14-040618.27	23.52	33.9	1.123 ± 0.319	Inconsistent
			J235639.17-040608.35	23.43	47.9	1.058 ± 0.186	Inconsistent

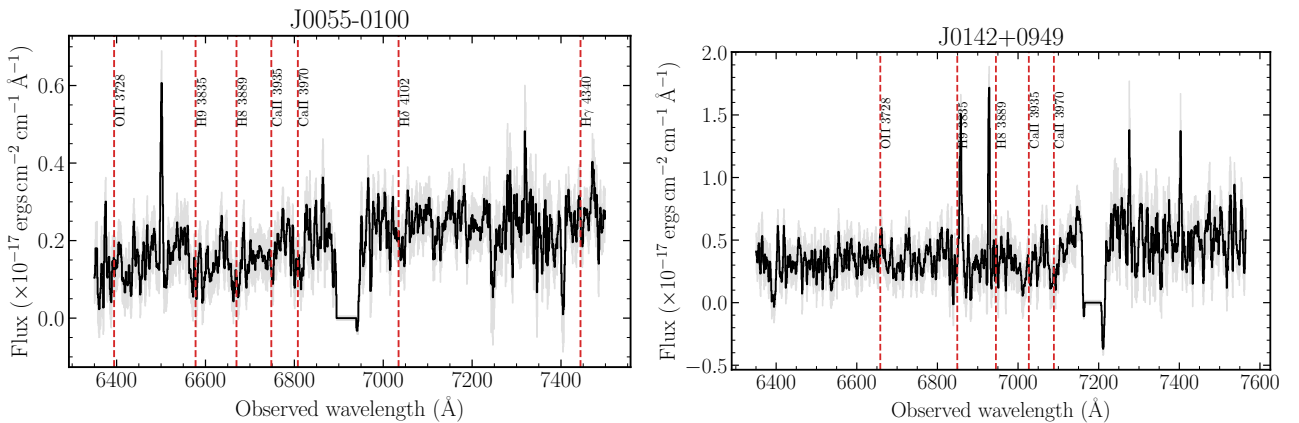


Figure B1. The spectra of the USMgII host galaxies, J0055–0100 and J0142+0949. Both of them are smoothed by 5 pixels, and both of them are identified based on the Ca II absorption present in their spectra. The vertical red dashed lines correspond to the Hydrogen Balmer lines and Ca II absorption lines corresponding to $z = 0.716$ (J0055–0100) and $z = 0.7858$ (J0142+0949).

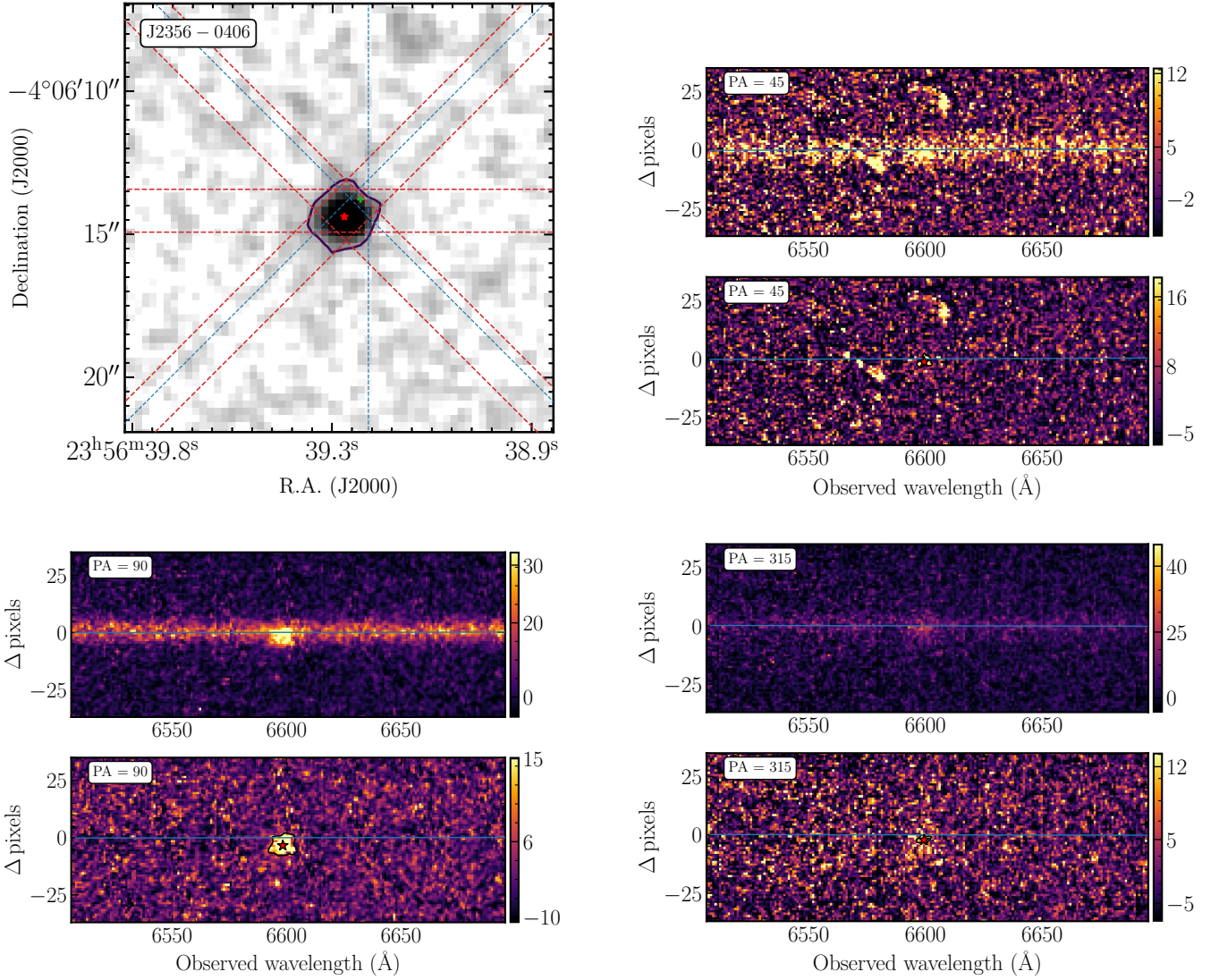


Figure C1. Illustration of the procedure to identify the impact parameter of the USMgII host galaxy towards the GOTOQ J2356-0406. The top left panel shows the zoomed-in observational configuration for the GOTOQ. The three pairs of red dashed lines show the three different slit configurations. The quasar centroid is marked with a red ‘*’. The blue dashed lines correspond to the physical shift along the spatial axis of the slit of the [O II] centroid from the central trace of the quasar. The most probable location of the USMgII host galaxy is marked with a green ‘+’. The top right, bottom left, and bottom right panels show the detection of [O II] emission and the associated shift of the [O II] emission from the central quasar trace. The central quasar trace is shown with a blue horizontal line, while the centroid of the [O II] emission is shown with a red ‘*’ in each of these three panels.

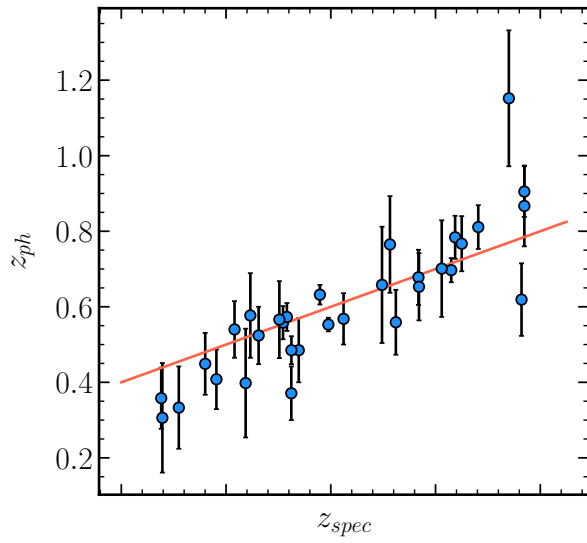


Figure C2. Comparison of the spectroscopic and photometric redshifts of the spectroscopically confirmed USMgII host galaxies. The orange line corresponds to the $z_{ph} = z_{sp}$